SCIENCE CHINA
Chemistry

• REVIEWS •
· SPECIAL TOPIC · Electrochemical Power Sources

December 2017 Vol.60 No.12:1508–1526
doi: 10.1007/s11426-017-9164-2

A review of solid electrolytes for safe lithium-sulfur batteries

Ying-Zhi Sun[1], Jia-Qi Huang[2], Chen-Zi Zhao[1] & Qiang Zhang[1*]

[1]*Beijing Key Laboratory of Green Chemical Reaction Engineering and Technology, Department of Chemical Engineering, Tsinghua University, Beijing 100084, China*
[2]*Advanced Research Institute Multidisciplinary Science, Beijing Institute of Technology, Beijing 100081, China*

Received August 31, 2017; accepted October 26, 2017; published online November 17, 2017

Due to the high specific capacity, low cost, and environmental friendliness, lithium-sulfur batteries hold great potential to become the mainstay of next-generation energy storage system. Regarding the composition of sulfur/carbon in cathode, flammable organic liquid electrolyte, and lithium metal anode, great concerns about the safety have been raised. Hence solid-electrolyte-based lithium-sulfur batteries, as one alternative route for safe batteries, are highly interested. This review highlights the recent research progress of lithium-sulfur batteries with solid electrolytes. Both sulfide solid electrolytes and oxide solid electrolytes are included. The sulfide solid electrolytes are mainly employed in all-solid-state lithium-sulfur batteries, while the oxide solid electrolytes are applied in hybrid electrolyte for lithium-sulfur batteries. The challenges and perspectives in this field are also featured on the basis of its current progress.

lithium-sulfur battery, inorganic solid electrolyte, ionic conductivity, lithium metal anode, composite sulfur cathode, high energy density energy storage system

Citation: Sun YZ, Huang JQ, Zhao CZ, Zhang Q. A review of solid electrolytes for safe lithium-sulfur batteries. *Sci China Chem*, 2017, 60: 1508–1526, doi: 10.1007/s11426-017-9164-2

1 Introduction

Rapid development of productivity substantially increased the energy demand. Under this circumstance, fossil energy is facing more and more challenges due to its non-renewability and pollution. The large-scale applications of clean and renewable energy, coming from solar, wind, geothermy, wave, and so on, are opening up new era based on green power [1,2]. Meanwhile, the explosive growth of portable electronics and automobiles make them a huge demand side of energy. Consequently, it is crucial to build an efficient bridge between renewable energy and these energy demanders through advanced energy storage [3–7]. High-energy-density rechargeable batteries play an important role in this key area. During the past thirty years, conventional lithium-ion batteries (LIBs) using ion-insertion materials (e.g. $LiFePO_4$ and $LiCoO_2$) as the cathode and graphite as the anode have been widely applied on consumer electronics [8]. However, low theoretical capacity of electrode materials limits further deployment of LIBs on emerging applications in electric vehicles and unmanned aerial vehicles [9]. Therefore, the exploitation of novel high-energy-density rechargeable battery systems are crucial to meet the demands [10–12].

The lithium-sulfur (Li-S) battery is one of the most promising rechargeable battery systems to make a breakthrough [13–16]. On the cathode side, the multi-electron conversion electrochemistry of sulfur leads to a theoretical capacity of 1672 mA h g^{-1}, which is much higher than that of ion-insertion cathode materials used in LIBs [17–19]. On the anode side, the lithium metal anode owns the lowest redox potential (−3.04 V vs. SHE, SHE=standard hydrogen electrode) and an ultra-high gravimetric capacity of 3860 mA h g^{-1}, which

*Corresponding author (email: zhang-qiang@mails.tsinghua.edu.cn)

is over ten times higher than that of the graphite anode (LiC_6, 372 mA h g^{-1}) [20]. In addition, the abundant mineral deposits of sulfur lead to its low price and make it possible to the widely application of Li-S batteries [21,22].

Besides the capacity and energy density based on advanced electrode [23–25] and separator [26–29], the safety of batteries is another considerable aspect for their widespread deployment. The flammability and possible leakage of organic liquid electrolytes (OLEs) are huge potential safety hazards for conventional rechargeable batteries as well as Li-S battery [30,31]. During the past two decades, the research of super ionic conductor has made great progresses. Under continuous researches and development, the room-temperature ionic conductivities of inorganic solid electrolytes (ISEs) are approaching, even surpassing, that of OLEs. The replacement of OLEs by ISEs is concerned a promising way to improve the safety of the battery [32,33]. The applications of ISEs introduce several merits for the Li-S batteries. Firstly, using ISEs is able to intrinsically avoid the dissolution of polysulfides and control the shuttle effect. Actually, in all-solid-state Li-S batteries, the electrochemical transformation will occur between sulfur and Li_2S directly instead of polysulfide generation. Secondly, the lithium ion transference number of ISEs is approaching 1, which is beneficial to the uniform deposition of lithium and restrain the formation of lithium dendrites. Besides, the ion transfer between ISEs and electrode does not involve desolvation, which may decrease the related activation barriers and accelerate the ion migration rate [34].

Despite many impactful reviews which have summarized the characterization of ISEs and their applications in rechargeable lithium batteries [35–40], none of them particularly focused on the Li-S batteries. Considering the special electrochemical property of Li-S battery, this review is to provide an overview of major research progresses in Li-S batteries with ISEs and extracts key points from these advancements. According to their different properties, the ISEs used in Li-S batteries can be divided into two categories: sulfide solid electrolytes (SSEs) and oxide solid electrolytes (OSEs). SSEs have relatively lower hardness and better interface contact, whose impedances of grain boundary and electrolyte/electrode interface are able to be decreased effectively through cold pressing. This advantage renders SSEs a good choice to fabricate all-solid-state Li-S batteries [41]. As for OSEs, due to their high hardness and bad interface contact, high temperature annealing (over 1000 K) is indispensable to decrease the interface impedance. Under such a high temperature, it is impossible to make solid cathode composition because of the complex reactions between sulfur, OSEs, and conductive additive. So, related researches mainly focus on combining OSEs with other materials, such as polymer and OLEs, to form hybrid electrolytes. This review aims to analyze the core issues of Li-S batteries with SSEs and OSEs respectively. A perspective on existing challenges and future directions is also presented.

2 Sulfide solid electrolyte

2.1 Introduction of sulfide solid electrolyte

Compared with O^{2-}, S^{2-} owns larger ionic radius. Substitution of O^{2-} in the OSEs by S^{2-} is able to effectively broaden the Li^+ transport bottleneck. In addition, S^{2-} also have better polarization capability than O^{2-}, which may weaken the interaction between Li^+ and anionic skeleton. Above characterizations are beneficial to the migration of lithium ion and leads to higher room temperature ionic conductivities of SSEs. According to the crystal structure and composition, we divided SSEs used in Li-S batteries into three categories: Li_2S-P_2S_5 glass and glass-ceramic, thio-LISICON, and anion-doped Li_2S-P_2S_5 (Table 1).

2.1.1 Li_2S-P_2S_5 glass and glass-ceramic

Li_2S-P_2S_5 glass is a kind of solid electrolyte that has received extensive attention for Li-S batteries. The formation of glass ceramic through annealing has been proposed to achieve high ionic conductivities. Hayashi *et al.* [44] synthesized glassy $80Li_2S{\cdot}20P_2S_5$ via high-energy ball milling P_2S_5 and Li_2S. The room-temperature ionic conductivity of this glassy powder was about 2×10^{-4} S cm^{-1}. After annealing under 250 °C, the room-temperature ionic conductivity of $80Li_2S{\cdot}20P_2S_5$ increased to 9×10^{-4} S cm^{-1}, which was attributed to the increase of crystallinity.

The ionic conductivities, crystallinity, and phase structures of Li_2S-P_2S_5 were strongly dependent on the annealing temperature. Taking $80Li_2S{\cdot}20P_2S_5$ as an example, after annealing under 240 °C, thio-LISICON phase (such as $Li_{3.25}P_{0.95}S_4$) was achieved with very high ionic conductivity. However, while increasing annealing temperature to 500 °C, the major compositions of $80Li_2S{\cdot}20P_2S_5$ glass-ceramic changed to Li_7PS_6 and Li_3PS_4 which were more thermodynamic stable but with lower ionic conductivity [43]. Mizuno *et al.* [42] found new phase generating when $70Li_2S{\cdot}30P_2S_5$ glass was annealed under 240 °C for 2 h. The as-synthesized $70Li_2S{\cdot}30P_2S_5$ glass-ceramic owned a high ionic conductivity of 3.2×10^{-3} S cm^{-1}. Tatsumisago *et al.* [62] further confirmed that such new phase was $Li_3P_3S_{11}$. They also reported that the crystallinity of $Li_3P_3S_{11}$ was able to be improved through increasing the annealing temperature to 360 °C. The $Li_3P_3S_{11}$ phase was converted into thermodynamic stable phase $Li_4P_2S_6$ when the annealing temperature was increased to 550 °C. The poor ionic conductivity of $Li_4P_2S_6$ (~10^{-6} S cm^{-1}) coincided with the obvious conductivity reduction of $70Li_2S{\cdot}30P_2S_5$ glass-ceramic after annealing under 550 °C.

Besides the intrinsic nature of Li_2S-P_2S_5 glass phase, the interfaces are also crucial to the ionic migration. Seino *et al.*

Table 1 Ion conductivities of different sulfide solid electrolytes

Composition	Classification	Conductivity at 25 °C (S cm^{-1})	Reference
$70Li_2S{\cdot}30P_2S_5$	Glass	5.4×10^{-5}	[42]
$75Li_2S{\cdot}25P_2S_5$	Glass	2.0×10^{-4}	[43]
$80Li_2S{\cdot}20P_2S_5$	Glass	2.0×10^{-4}	[44]
$80(0.7Li_2S{\cdot}0.3P_2S_5){\cdot}20LiI$	Glass	5.6×10^{-4}	[45]
$95(0.8Li_2S{\cdot}0.2P_2S_5){\cdot}5LiI$	Glass	2.7×10^{-3}	[46]
$56Li_2S{\cdot}24P_2S_5{\cdot}20Li_2O$	Glass	$>1.0\times10^{-4}$	[47]
$75Li_2S{\cdot}21P_2S_5{\cdot}4P_2O_5$	Glass	$>1.0\times10^{-4}$	[48]
$67.5Li_2S{\cdot}7.5Li_2O{\cdot}25P_2S_5$	Glass	1.1×10^{-4}	[49]
$33(0.7B_2S_3{\cdot}0.3P_2S_5){\cdot}67Li_2S$	Glass	1.4×10^{-4}	[50]
$67(0.75Li_2S{\cdot}0.25P_2S_5){\cdot}33LiBH_4$	Glass	1.6×10^{-3}	[51]
$70Li_2S{\cdot}30P_2S_5$	Glass-Ceramic	3.2×10^{-3}	[42]
$80Li_2S{\cdot}20P_2S_5$	Glass-Ceramic	9×10^{-4}	[44]
$80Li_2S{\cdot}20P_2S_5$	Glass-Ceramic	7.4×10^{-4}	[43]
$Li_7P_3S_{11-z}$	Glass-Ceramic	5.4×10^{-3}	[52]
$Li_7P_3S_{11}$	Glass-Ceramic	1.7×10^{-2}	[53]
$Li_{3.25}P_{0.95}S_4$	Glass-Ceramic	1.3×10^{-3}	[54]
γ-Li_3PS_4	Crystalline	3.0×10^{-7}	[55]
β-Li_3PS_4	Crystalline	1.6×10^{-4}	[56]
$Li_{3.25}Ge_{0.25}P_{0.75}S_4$	Crystalline	2.2×10^{-3}	[57]
$Li_{10}GeP_2S_{12}$	Crystalline	1.2×10^{-2}	[58]
$Li_{10}SnP_2S_{12}$	Crystalline	4.0×10^{-3}	[59]
$Li_{11}Si_2PS_{12}$	Crystalline	$>1.2\times10^{-2}$	[60]
$Li_7P_2S_8I$	Crystalline	6.3×10^{-4}	[61]

[53] compacted the $70Li_2S{\cdot}30P_2S_5$ glass powder under a high pressure of 94 MPa and annealed it at 280 °C for 2 h. Compared with the $70Li_2S{\cdot}30P_2S_5$ glass-ceramic after simple cold pressing, the inner gap and grain boundary of as-synthesized $70Li_2S{\cdot}30P_2S_5$ glass-ceramic significantly reduced, which improved the interface transmission condition of Li^+. Consequently, an extra-high ionic conductivity of 1.7×10^{-3} S cm^{-1} was achieved, which was even higher than the conductivity of conventional liquid electrolyte.

2.1.2 Thio-LISICON

Thio-LISICON is one of the most typical crystal phase SSEs. The general chemical formula of thio-LISICON is $Li_{4-x}A_{1-y}B_yS_4$ (A=Si, Ge , B=Zn, Al, Pt). It was firstly reported by Kanno and co-workers [63]. Several thio-LISICON phases (e.g. Li_2S-GeS_2, Li_2S-GeS_2-ZnS and Li_2S-GeS_2-Ga_2S_3) have been fabricated and their ionic conductivities were explored. The aliovalent substitution improves the ionic conductivity effectively. Li_4GeS_4 exhibits a low room temperature ionic conductivity of 2×10^{-7} S cm^{-1}. However, after the substitution of $Ge^{4+}\rightarrow Ga^{3+}+Li^+$, $Li_{4.275}Ge_{0.61}Ga_{0.25}S_4$ presents an ionic conductivity as high as 6.5×10^{-5} S cm^{-1} at ambient temperature [63]. On this basis, Kanno *et al.* [57] further obtained thio-LISICON $Li_{4-x}Ge_{1-x}P_xS_4$ ($0<x<1.0$) through the substitution of $Ge^{4+}+Li^+\rightarrow P^{5+}$. According to the crystal structure, thio-LISICON $Li_{4-x}Ge_{1-x}P_xS_4$ could be divided into three composition regions: region I ($0<x\leq0.6$), region II ($0.6<x\leq0.8$), and region III ($0.8<x<1.0$). Particularly, the thio-LISICON phase in region II ($0.6<x\leq0.8$) showed much higher room temperature ionic conductivities over 10^{-3} S cm^{-1} and owned special monoclinic superstructures. Compared with Li_4GeS_4, higher conductivities of thio-LISICON $Li_{4-x}Ge_{1-x}P_xS_4$ were attributed to more Li^+ vacancies created by aliovalent substitutions.

A thio-LISICON type lithium superionic conductor, $Li_{10}GeP_2S_{12}$, was reported to own an extra high room temperature ionic conductivity (1.2×10^{-2} S cm^{-1}) which was comparable to those of liquid electrolytes. The crystal structure of $Li_{10}GeP_2S_{12}$ is shown in Figure 1(a, b). The three-dimension framework of $Li_{10}GeP_2S_{12}$ is made up of $(Ge_{0.5}P_{0.5})S_4$ tetrahedron, PS_4 tetrahedron, LiS_4 tetrahedron and LiS_6 octahedra. There are two kinds of tetrahedral sites (4d and 2b) and three kinds of lithium sits (16h, 4d and 8f) in the unit cell. The 4d tetrahedral sites are occupied by Ge and P. The 2b tetrahedral sites, which are smaller, are occupied by P solely. $(Ge/P)S_4$ tetrahedron and LiS_6 octahedron form the 1D chain along *c* axis by sharing a common edge. The 1D chains are connected to form the three-dimensional framework through PS_4 tetrahedron which shares a common

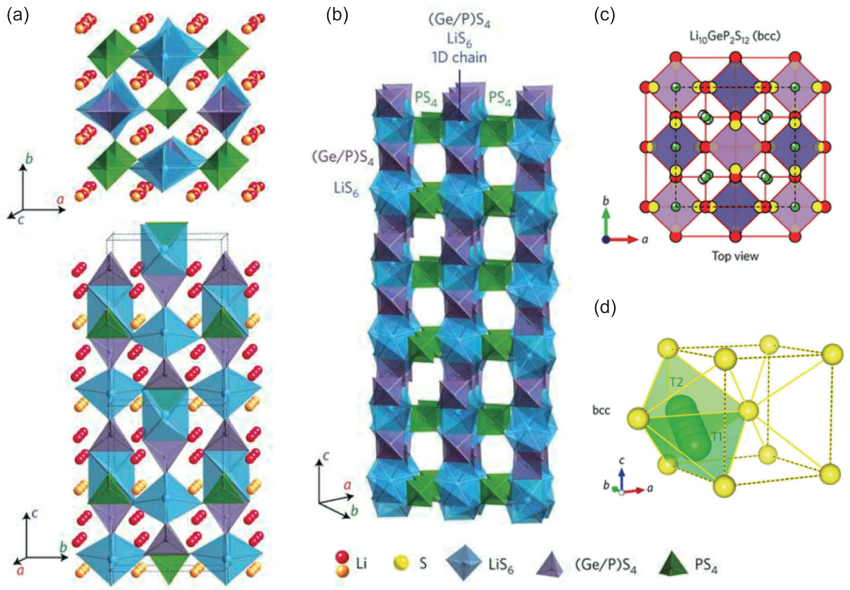

Figure 1 Sulfide solid state electrolytes. (a) The framework structure and lithium ions that participate in ionic conduction. (b) Framework structure of $Li_{10}GeP_2S_{12}$. Reprinted with permission from Ref. [58], copyright 2011, Nature Publishing Group. (c) Crystal structure of Li-ion conductors $Li_{10}GeP_2S_{12}$. Li atom, partially occupied Li atom, S atom, PS_4 tetrahedral, and GeS_4 tetrahedral (partially occupied in $Li_{10}GeP_2S_{12}$) are colored green, green-white, yellow, purple and blue, respectively. (d) Li-ion migration path in BCC sub-lattice. Li^+ and S^{2-} are colored green and yellow respectively. Reprinted with permission from Refs. [64], copyright 2015, Nature Publishing Group (color online).

corner with LiS_6 octahedron. The pathway of lithium ion is fabricated by LiS_4 tetrahedron in the 8f and 16h sites through sharing a common edge [58]. Wang *et al.* [64] predicted that $Li_{10}GeP_2S_{12}$ had a body-centered cubic (BCC) anion sublattice. In the BCC lattice, Li^+ migrate from one tetrahedral site to another face-sharing tetrahedral site. Such T-T pathway has low activation barrier, which benefits to the rapid migration of Li^+.

Although Li_2S-GeS_2-P_2S_5 thio-LISICONs have extra high room temperature ionic conductivity, their poor compatibilities with lithium metal and the high costs of germanium hindered their practical applications [65]. To overcome these drawbacks, other sulfides, such as SnS_2 and SiS_2, were considered to substitute GeS_2 and to render ultrafast superionic conductors. For the Li_2S-SnS_2-P_2S_5 system, the doped Sn was really rare in the thio-LISICON phase. Consequently, the improvement on ionic conductivity was not significant. While for the Li_2S-SiS_2-P_2S_5 system, much more Si could be doped in the solid solution. It was attributed to the smaller size of Si^{4+} that allows Si^{4+} occupy 2b tetrahedral sites. Additionally, after substituting P^{5+} with Si^{4+}, the concentrate of Li^+ was increased due to the charge-compensation, resulting in higher ionic conductivity [66].

2.1.3 Anion-doped Li_2S-P_2S_5

Doping another anion is also an effective way to increase the conductivity of glassy electrolytes, which is called "mixed-anion effect". As early as 1981, Mercier *et al.* [67] reported that the addition of lithium halide (LiX, X=Cl, Br, I) contributes to the improvement of the ionic conductivity of Li_2S-P_2S_5 glass. The ionic conductivity was positively related with the polarizability of the halide ($\sigma_{LiI}>\sigma_{LiBr}>\sigma_{LiCl}$). Ujiie *et al.* [45,46] further investigated that in the $(100-x)(0.7Li_2S\cdot0.3P_2S_5)\cdot xLiI$ glass, the ionic conductivity increased as the LiI content increasing in the $(100-x)(0.7Li_2S\cdot0.3P_2S_5)\cdot xLiI$ glass-ceramic, the introduction of LiI obviously decreased the ionic conductivity. While in the $(100-x)(0.8Li_2S\cdot0.2P_2S_5)\cdot xLiI$ glass-ceramic, the ionic conductivity climbed up and then declined as the LiI content increasing, the room temperature ionic conductivity peaked (2.7×10^{-3} S cm^{-1}) when the x=5.

In addition, suitable anion doping could also improve the stabilities of SSEs. Rangasamy *et al.* [61] reported that a new phase ($Li_7P_2S_8I$) was obtained through mixing β-Li_3PS_4 and LiI with subsequent heat treatment. Although the room temperature ionic conductivity of as-synthesized $Li_7P_2S_8I$ is not very high (6.3×10^{-4} S cm^{-1}), $Li_7P_2S_8I$ exhibited an extremely high electrochemical stability window with up to 10 V vs. Li/Li^+. It was advised that the I^- was effectively integrated into the solid solution, which avoids the oxidation of I^-. On the other hand, the existence of I^- improved the compatibility between SSEs and lithium metal, which was crucial for the practical applications of SSEs in lithium metal batteries.

Most of SSEs are sensitive to moisture, indicating that their preparation and application cannot be handled in the air directly. To overcome this drawback, numerous researches have been explored on partially replacing S with O to improve the stability of SSEs against moisture. Ohtomo *et al.* [47] reported that partial substitution of Li_2O for Li_2S in $70Li_2S\cdot30P_2S_5$ was able to suppress the generation of

H_2S. Hayashi *et al.* [48] described that partially replacing P_2S_5 with P_2O_5 decreased the H_2S generation rate. However, such kind of substitution introduced PO_4 units and oxysulfide units. The non-bridging oxides may trap Li^+ strongly, which led to the decrease of the ionic conductivity. Further investigations are still essential to improve the stability of SSEs in moisture atmosphere but not at the cost of the ionic conductivity.

2.2 Research progress on cathode side

Many SSEs with high ionic conductivities have been explored on the cathode side of all-solid-state Li-S batteries owning to their low hardness, good interface contact, as well as the feasibility in fabrication of SSEs with high ionic conductivities through cold pressing.

In general, sulfur cathode presents three major drawbacks: (1) the ionic conductivities and electronic conductivities of active sulfur and discharge product Li_2S are too low; (2) the transition from S to Li_2S is accompanied by huge volume expansion (~79%) that can destroy the electrode structure; (3) soluble high order polysulfides are produced during the charge and discharge process in routine organic liquid electrolytes. They diffuse to anode side and react with lithium metal to produce low order polysulfides [68–70]. Low order polysulfides are able to diffuse back to cathode side, react with sulfur and generate high order polysulfides again. Such phenomenon, which is called shuttle effect, will induce capacity loss and efficiency decrease [13,15,19,26].

Although the substitution of organic liquid electrolyte with solid electrolyte is able to avoid the shuttle effect, the other two problems become more prominent. Due to the immobility of solid electrolytes, the huge volume change during charge-discharge process will destroy not only the electron pathway but also the ion diffusion channels. Additionally, the absence of soluble redox intermediate (high order polysulfides) further aggravates the impact of the poor ionic conductivities and electronic conductivities of S and Li_2S. Therefore, it is crucial to build efficient ion-electron pathway and optimize the ion-electron transfer among active materials, solid electrolytes, and conductive agents in all-solid-state Li-S batteries. The recent advances in the use of SSEs and conductive additives to fibrate the cathodes of all-solid-state Li-S batteries has been described in Table 2. Significant progress has been achieved on the capacity and cycling performance. The efficient ion transport between active materials and SSEs is emphatically analyzed in the following section.

Nano-crystallization and using nanostructure are important methods to increase the ion transport between active materials and solid electrolytes. On the one hand, the ultrahigh surface area of nanostructure allows active materials contact with solid electrolytes sufficiently. On the other hand, the

Table 2 The performances of Li-S batteries with different SSEs

Solid electrolyte	Conductivity at 25 °C (S cm^{-1})	Conductive agent	Composition of cathode	Current density (mA cm^{-2})	Capacity (mA h g^{-1})	Reference
$60Li_2S{\cdot}40P_2S_5$	2×10^{-5}		S/C/SE=50/10/40	6.4	1096 (1st)	
$60Li_2S{\cdot}40P_2S_5$	2×10^{-5}	Ketjen black	S/C/SE=50/10/40	0.64	1568 (1st)	[71]
$80Li_2S{\cdot}20P_2S_5$	5×10^{-4}		S/C/SE=50/10/40	6.4	565 (1st)	
$80Li_2S{\cdot}20P_2S_5$ glass	2.2×10^{-4}	MCMB+Super P	S/C/SE=5/15/2	0.074	~400 (20th)	[72]
$80Li_2S{\cdot}20P_2S_5$ glass-ceramic	$\sim10^{-3}$	Acetylene black	Li_2S/C/SE=25/25/50	0.064	~700 (1st)	[73]
$80Li_2S{\cdot}20P_2S_5$ glass-ceramic	$\sim10^{-3}$	Acetylene black	S/C/SE=25/25/50	1.3	850 (200th)	[74]
$80Li_2S{\cdot}20P_2S_5$ glass-ceramic	$\sim10^{-3}$	Acetylene black	S/C/SE=50/21/29	0.064	1050 (50th)	[75]
Li_3PS_4	$\sim10^{-4}$	CNF	S/C/SE=30/10/60	0.025	~1500 (10th)	[76]
Li_3PS_{4+5}	3×10^{-5}	WVA-1500	Li_3PS_{4+5}/C=2/1	0.036	700 (300th)	[77]
P_2S_5+ $0.82(Li_{1.5}PS_{3.3})\cdot$ $0.18LiI$	3.1×10^{-4}	Acetylene black	S/PS/C/SE=50/10/10/30	1.3	~1400 (100th)	[78]
Li_6PS_5Br	$\sim10^{-3}$	Super P	S/C/SE=20/10/70	0.38	1080 (50th)	[79]
Li_6PS_5Cl + $80Li_2S{\cdot}20P_2S_5$ glass-ceramic	4×10^{-4} 1.3×10^{-3}	Carbonized PVP + Carbon black	Li_6PS_5Cl-Li_2S-C/CB/$80Li_2S{\cdot}20P_2S_5$=60/10/30	0.18	1190 (60th)	[80]
$Li_{3.25}Ge_{0.25}P_{0.75}S_4$	$(2–4)\times10^{-3}$	Acetylene black	S/C/SE=9.25/25/50	0.013	~ 900 (10th)	[81]
$Li_{3.25}Ge_{0.25}P_{0.75}S_4$	$(2–4)\times10^{-3}$	CMK-3	S/C/SE=15/35/50	0.023	~1000 (50th)	[82]
$Li_{3.25}Ge_{0.25}P_{0.75}S_4$	$(2–4)\times10^{-3}$	Carbon replica CR12	S/C/SE=15/35/50	0.065	366 (20th)	[83]

poor conductivities of S and Li_2S limit the depth of the electrochemical reaction, thus nano-crystallization is able to significantly improve the utilization of active materials.

Nagao *et al.* [73] fabricated the composite cathodes through the pre ball milling of Li_2S. As-prepared Li_2S nanoparticles owned a size of ~500 nm and uniformly dispersed in the solid electrolytes and conductive additives. There was no obvious agglomeration of Li_2S nanoparticles after charge-discharge cycling (Figure 2(a–d)). Under a current density of 0.064 mA cm^{-1} (0.035 C), this kind of cathode achieved a reversible capacity of 1000 mA h g^{-1}. Compared with the normal cathode composition without pre ball milling, it was found that reducing the size of active materials had effective influence on improving the capacity, especially under a high current density. While increasing the current density to 6.4 mA cm^{-2}, the cathode composition with Li_2S nanoparticles still held a capacity of 271 mA h g^{-1} but the normal cathode composition only remained a capacity of 70 mA h g^{-1}(Figure 2(e)). Nagao *et al.* [75] further prepared the cathode composition by mechanical milling under 155 °C, which reduced the size of Li_2S nanoparticle to less than 200 nm. On this basis, cathode composition of which sulfur content reached up to 50% was made. In spite of such a high sulfur content, as-prepared cathode composition presented really high reversible capacity and cycle stability. A capacity of 1050 mA h g^{-1} was achieved after 50 cycles under 0.064 mA cm^{-2}. In comparison, the cathode composition prepared under room temperature only had an initial capacity of ~550 mA h g^{-1}. A Li_2S/vapor grown carbon fiber cathode are intergrated with $78L_2S{\cdot}22P_2S_5$ into a solid state Li-S battery with a high capacity of 600 mA h g^{-1}, 100% coulombic efficiency, and a life of 20 cycles [84]. A MoS_2 doped Li_2S-P_2S_5 electrolyte with an ionic conductivity of 4.8 mS cm^{-1} was applied in an all-solid-state cell with a discharge capacity of 1020 mA h g^{-1} [85].

On account of the immobility of solid electrolytes together with the poor conductivity of Li_2S and S, the ion diffusion channels and electron pathway are separated, which indicates lithium ions are difficult to reach the active sites where electrochemical reactions occur. This leads to local charge accumulation and block consequent reactions. Nanoparticles are able to contact both solid electrolytes and conductive additives in a small local area, which therefore overcome the barrier and achieve mixed conducting of ion and electron. Han *et al.* [80] described an effective bottom-up method to obtain nano-sized mixture of active materials, solid electrolytes, and conductive framework for the ion-electron mixed conducting. Polyvinylpyrrolidone, Li_6PS_5Cl, and Li_2S are dissolved in ethanol with subsequent co-precipitation and high temperature carbonization. The Li_2S and Li_6PS_5Cl are uniformly dispersed in the carbon framework in the form of nanoparticles (Figure 3(a, b)). The size of Li_2S and Li_6PS_5Cl are around 4 nm. The high-resolution transmission electron microscope (TEM) images (Figure 3(c, d)) confirmed the existence of ion-electron mixed conducting area in as-prepared nanocomposite cathode. Both Li_2S-Li_6PS_5Cl-C and Li_2S-C composites were employed in cathode. The Li_2S-Li_6PS_5Cl-C cathode fabricated through mixing with carbon black and $80Li_2S$-$20P_2S_5$ exhibited lower overpotential than Li_2S-C cathode (Figure 3(e)), indicating the ion-electron mixed conducting was able to improve the kinetics of redox reactions in the electrode. In addition, the existence of ion-electron mixed conducting pathways also improved the utilization of active materials. Under a current density of 50 mA g^{-1}, the initial capacity of Li_2S-C cathode was only 489 mA h g^{-1} (the capacity in this work was calculated based on the mass of Li_2S). After 20 cycles, the capacity rapidly declined to 49 mA h g^{-1}. In comparison, the capacity of Li_2S-Li_6PS_5Cl-C cathode achieved 648 mA h g^{-1} initially and held at 830 mA h g^{-1} after 60 cycles (Figure 3(f)) [80].

Recently, Xu and co-workers [86] coated a nanolayer (~2 nm) amorphous sulfur on the reduced graphene oxide (rGO) (Figure 4(a–d)) and then uniformly distributed as-prepared rGO@S composition into superionic conductor $Li_{10}GeP_2S_{12}$ and acetylene black (AB) to fabricated all-solid-state cathode. This design, on one hand, reduced the interfacial resistance and achieved high ionic and electronic conductivities, which improved the utilization of sulfur. On the other hand, the uniform distribution of rGO@S nano-composition significantly minimized the stress/strain during cycling and protected the cathode structure. The all-solid-state Li-S batteries, which employed an rGO@S-$Li_{10}GeP_2S_{12}$-AB cathode, $Li_{10}GeP_2S_{12}$/75%Li_2S-24%P_2S_5-1%P_2O_5 bilayer solid electrolyte and lithium metal anode, showed an excellent electrochemical performance approaching conventional Li-S batteries with OLEs. There was no obvious capacity decay with a high coulombic efficiency of ~100% during the first 30 cycles at 0.05 C (Figure 4(e)). At 60 °C, high rate capacities of 1525.6, 1384.5, 1336.3, 903.2, 502.6 and 204.7 mA h g^{-1} were obtained at 0.05, 0.1, 0.5, 1.0, 2.0 and 5.0 C respectively (Figure 4(f)). A high and reversible capacity of 830 mA h g^{-1} was also achieved at 1.0 C for 750 cycles.

The superiority of nanostructures mainly comes from their ultrahigh surface area, the intrinsic migration rate on the interface of solid electrolyte and sulfur is not improved. To further increase the ion conductivity of solid state cathode composition, several routes have been proposed in order to optimize the interface ion migration. Nagata *et al.* [71] compared the capacities of all-solid-state Li-S batteries with different SSEs. They found that the capacities were not totally positively related with the conductivities of SSEs. Although the conductivity of $Li_{1.3}PS_{3.3}$ (2×10^{-5} S cm^{-1}) is much lower than that of $Li_{4.0}PS_{4.5}$ (5×10^{-4} S cm^{-1}), the capacity of Li-S battery with $Li_{1.3}PS_{3.3}$ (1096 mA h g^{-1}) is much higher than that with

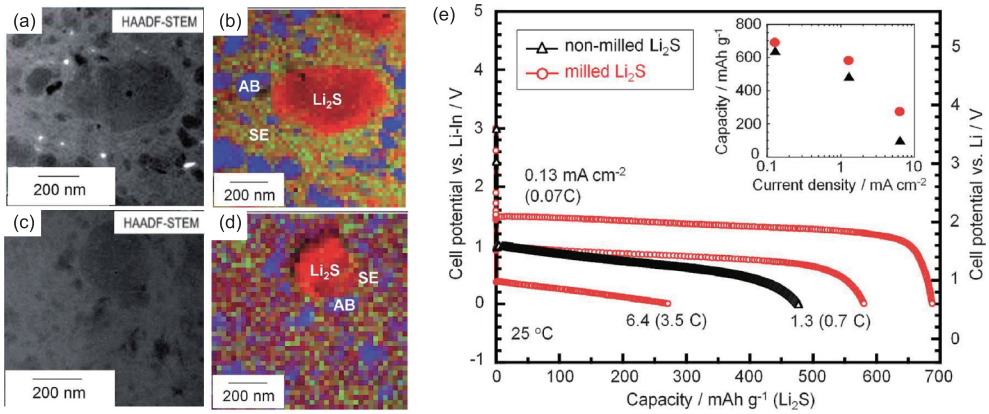

Figure 2 Li_2S composite electrode. (a) Cross-sectional high angle annular dark field scanning transmission electron microscopy (HAADF-STEM) image and (b) corresponding EELS map of nano-Li_2S composite electrodes after 10 cycles; (c) cross-sectional HAADF-STEM image and (d) EELS maps of electrodes before charge-discharge test; (e) discharge curves and capacities of all-solid-state lithium-sulfur batteries with nano-Li_2S composite electrode and normal electrode at different current densities. Reprinted with permission from Ref. [73], copyright 2012, Royal Society of Chemistry (color online).

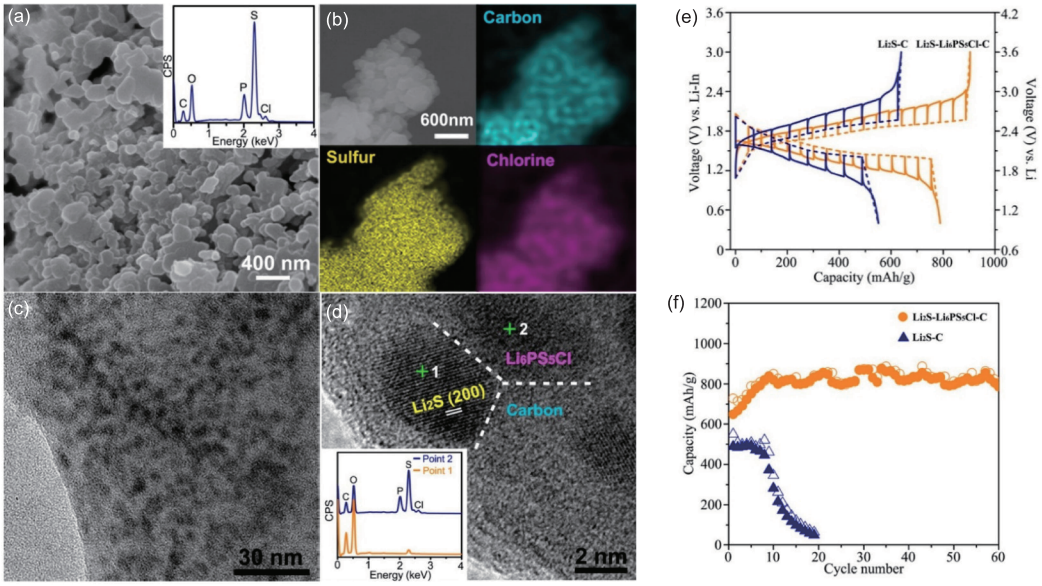

Figure 3 Li_2S-Li_6PS_5Cl-C electrode. (a) Scanning electron microscopy (SEM) image of the Li_2S-Li_6PS_5Cl-C nanocomposite. The inset shows the energy-dispersive X-ray spectroscopy (EDS) result. (b) The elemental mappings of carbon, sulfur, and chlorine in the composite. (c) The TEM image of the Li_2S-Li_6PS_5Cl-C nanocomposite. (d) The high-resolution TEM image of the Li_2S-Li_6PS_5Cl-C nanocomposite, and the inset shows the EDS results at point 1 and point 2, respectively. (e) Equilibrium (open-circuit)-voltage (dashed lines) and transient voltage (solid lines) profiles versus capacity for the 1st cycle of the Li_2S-C and Li_2S-Li_6PS_5Cl-C nanocomposite electrodes. (f) Cycling performances of the Li_2S-C and Li_2S-Li_6PS_5Cl-C nanocomposite electrodes at 50 mA g^{-1}. Reprinted with permission from Ref. [80], copyright 2016, American Chemical Society (color online).

$Li_{4.0}PS_{4.5}$ (565 mA h g^{-1}). They speculated that such abnormal phenomenon was attributed to the activation of $Li_{1.3}PS_{3.3}$ to sulfur. They further combined $0.82(Li_{1.5}PS_{3.3})\cdot0.18(LiI)$ with P_2S_5 to fabricate composite electrolyte. $0.82(Li_{1.5}PS_{3.3})\cdot0.18(LiI)$, which owned an ultrahigh ionic conductivity of 3.1×10^{-3} S cm^{-1}, was responsible forming ion pathway and P_2S_5 was in charge of activing sulfur. As-prepared composite cathode showed an ultrahigh initial capacity of 1550 mA h g^{-1}. A capacity of ~1400 mA h g^{-1} was able to be maintained after 100 cycles [78]. Although excellent performance was achieved, the concept of activation was too ambiguous. Nagata *et al.* [71] did not clearly explain the reason for the activation of P_2S_5. According to following researches, we gave a particular explanation here. Li_2S reacted with P_2S_5 and *in situ* formed Li_3PS_4 on the surface. Li_3PS_4 owned a high ionic conductivity and the *in-situ* formation process helps to optimize the contact between Li_2S and Li_3PS_4. Under this situation, the interface ion migration rate was accelerated significantly, making full use of the active materials.

The electrochemical performance of a working cell can be realized through the increased the interface ion migration rate benefited from the nanostructured electrode. For instance, Lin *et al.* [87] explored a nanocomposite Li_2S electrode. In

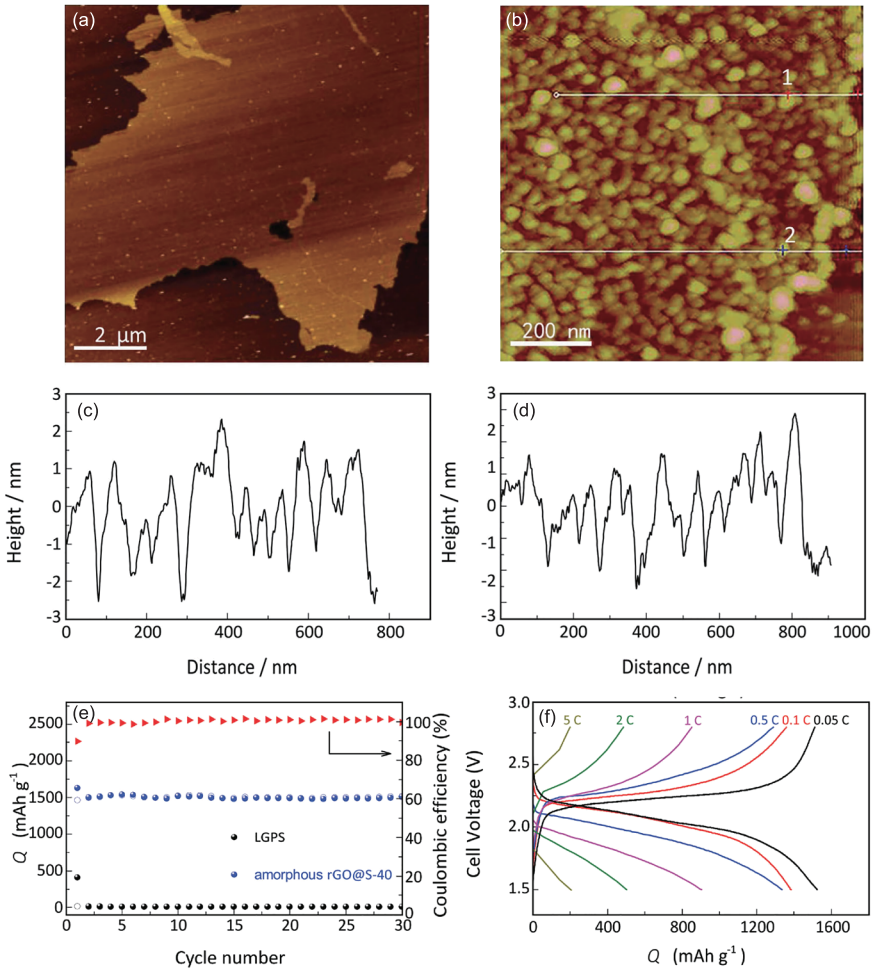

Figure 4 All solid state Li-S batteries with rGO@S cathode. AFM images of (a, b) amorphous rGO@S-40 composite on a Si substrate and corresponding height profiles at (c) Line 1 and (d) Line 2 in (b). (e) Cycling performances of the amorphous rGO@S-40 composite by subtracting the $Li_{10}GeP_2S_{12}$ contribution. (f) Galvanostatic discharge/charge profiles for the amorphous rGO@S-40 composite in all solid-state Li-S battery under different C rates at 60 °C. Reprinted with permission from Ref. [86], copyright 2017, Wiley-VCH (color online).

details, S reacted with $Li(CH_2CH_3)_3BH$ in tetrahydrofuran (THF) to form Li_2S nano particles. The as-prepared nano-Li_2S then reacted with P_2S_5 directly and was covered with a Li_3PS_4 shell into lithium superionic sulfide cathode (LSS cathode, Figure 5(a)). The room temperature ionic conductivity of nano-Li_2S raised about four orders of magnitude (Figure 5(b)), which proved that the solid electrolyte shell significantly increased the ion migration rate. The cathode using such Li_3PS_4 covered nano-Li_2S exhibited a high initial discharge capacity of 848 mA h g^{-1} (the capacities in this work were all based on the mass of Li_2S) and maintained ~594 mA h g^{-1} after 100 cycles at 0.1 C under 60 °C. In comparison, the cathode using normal nano-Li_2S only rendered an initial discharge capacity of 569 and 402 mA h g^{-1} after 100 cycles (Figure 5(c)). Additionally, comparing their charge-discharge curve, it could be found that the batteries using Li_3PS_4 covered nano-Li_2S as cathode exhibited lower overpotential (Figure 5(d)), which was ascribed to the higher interface ion migration rate [87].

Besides raising the interface ion migration rate, it is also important to improve the ionic conductivities of active materials (S and Li_2S). According to Lin *et al.*'s work [77], S was able to react with Li_3PS_4 in THF to form lithium polysulfidophosphates Li_3PS_{4+n} ($0<n<9$) (Figure 6(a)). As-prepared lithium polysulfidophosphates owned an ionic conductivity of 3×10^{-5} S cm^{-1} at 25 °C, which was much higher than those of S and Li_2S (~10^{-13} S cm^{-1}) (Figure 6(c)). Due to the outstanding ionic conductivity, Li_3PS_{4+5} was able to act both active materials and solid electrolyte. The all-solid-state Li-S batteries employing Li_3PS_{4+5} as cathode composition delivered high capacities and excellent cycle stabilities. A discharge capacity of 1272 mA h g^{-1} at 0.1 C was achieved for the first cycling at room temperature. The capacity stabilizes at ~700 mA h g^{-1} after 300 cycles. At 60 °C, higher initial capacities of ~1400 mA h g^{-1} and stable capacities of ~1200 mA h g^{-1} were obtained (Figure 6(d)). According to the result of Raman spectra (Figure 6(e)), it was believed that there were breakage and reformulation of S–S bond during

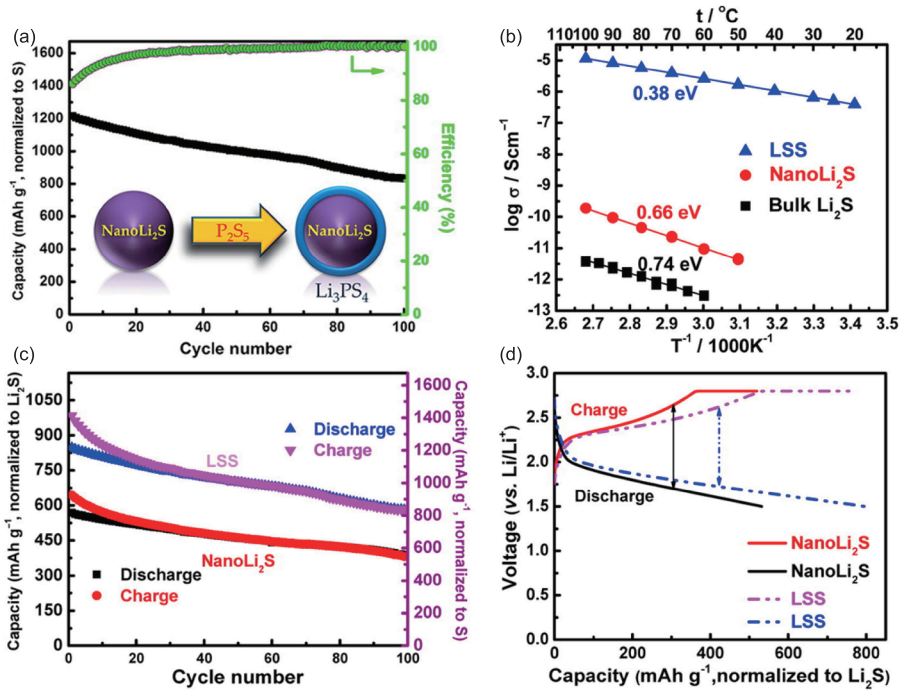

Figure 5 Lithium superionic sulfide cathode (LSS cathode). (a) The cycling performance at 0.1 C. The inset is the scheme of the forming process of Li_3PS_4 coating. (b) Temperature dependency of ionic conductivities of the bulk Li_2S, nano-Li_2S, and LSS. (c) The cycling performances and (d) voltage-capacity profiles of nano-Li_2S cathode and LSS cathode [87]. Reprinted with permission from Ref. [87], copyright 2013, American Chemical Society (color online).

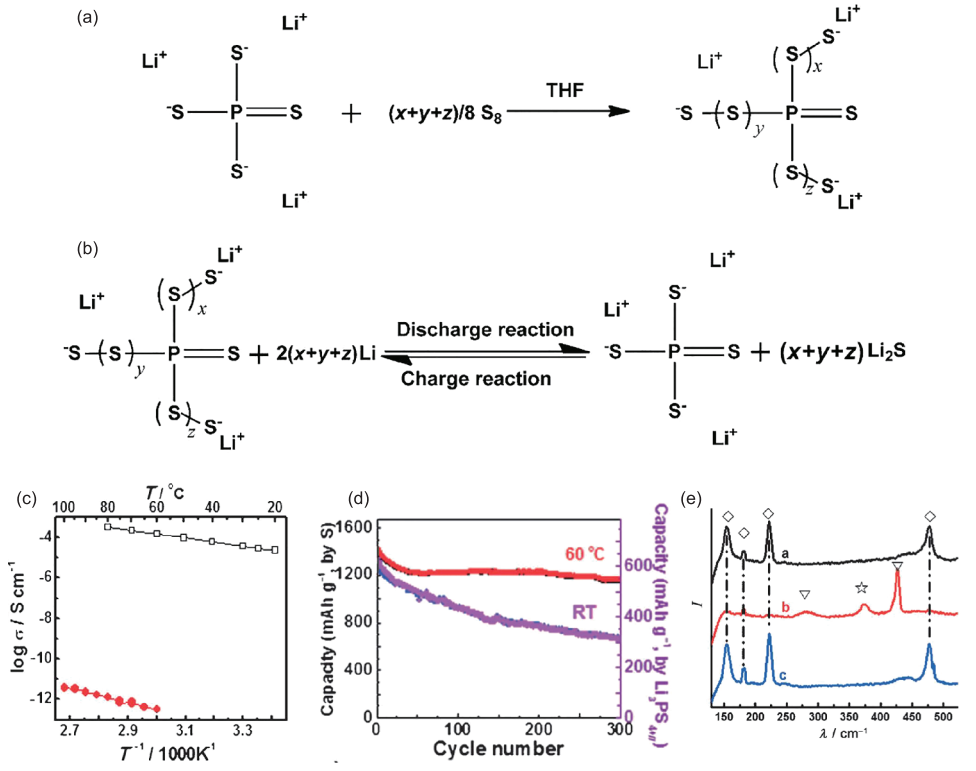

Figure 6 Li_3PS_{4+5} electrolyte. (a) Reaction of sulfur with Li_3PS_4 yields Li_3PS_{4+n} in THF. (b) The electrochemical reaction mechanism for charge and discharge of Li_3PS_{4+n} (reversible scission and formation of S–S bonds). (c) Temperature dependency of ionic conductivity of Li_3PS_{4+5} and Li_2S. (d) The cycling performance of Li_3PS_{4+5} cathode at the rate of 0.1 C at room temperature and 60 °C (pink/red: charge; black/blue: discharge). (e) Raman spectra of the Li_3PS_{4+5} electrode before cycling (black line), at the end of first discharge cycle (red line), and at the end of first charge cycle (blue line). ◇: peaks from the S–S bond in Li_3PS_{4+5}; ▽: peaks from the P–S bond in Li_3PS_4; ☆: the peak of Li_2S. Reprinted with permission from Ref. [77], copyright 2013, Wiley-VCH (color online).

charge and discharge, which partially proved that the conversion between Li_2S, Li_3PS_4 and Li_3PS_{4+n} was reversible during the cycling [77]. Tanibata *et al*. [88] described amorphous P_2S_{5+x} species can be achieved through mechanically milling S, P_2S_5 and Ketjen black, and the as-obtained all-solid-state Li-S batteries exhibited a capacity of 942 mA h g^{-1} at 0.64 mA cm^{-2}. Recently, Tu and co-workers [89] described a $Li_7P_{2.9}Mn_{0.1}S_{10.7}I_{0.3}$ glass-ceramic electrolyte with an ionic conductivity of 5.6 mS cm^{-1}, which afforded a Li-S cell with a large capacity of 796 mA h g^{-1} at 0.05 C. Liu and co-workers [90] proposed a polyethylene glycol-graphene oxide mixture as solid electrolyte for an all-solid-state lithium-sulfur battery. The cell exhibits a high initial discharge capacity of 1225 mA h g^{-1} at 0.2 C and good cycling stability with a retention of 86.6% after 100 cycles at 2 C and 80 °C.

2.3 Research progress on anode side

Lithium metal anode is another grand challenge for the development of Li-S batteries [91–93]. The research on lithium metal anode can be traced back to 1970s [94]. However, there is still a long way to perfectly solve the problems of lithium metal anode [95,96]. Lithium metal is considered as an ideal anode material due to its high theoretical specific capacity of 3860 mA h g^{-1} and lowest redox potential of −3.04 V vs. SHE [97]. However, there are many drawbacks on Li metal anode in a working cell. The uneven plating/stripping of lithium induces the formation of dendrites [98,99]. Dendrites may pierce the separator and lead to internal short circuit. Additionally, lithium metal is unstable with the conventional OLEs used in Li-S batteries. On the one hand, the reactions between lithium and organic liquid electrolyte reduce the cycle efficiency of lithium metal anode [100]. On the other hand, excess electrolyte is needed due to the continuous dissipation, which reduces the capacity density of the whole battery [31,101,102]. In all-solid-state Li-S batteries, the above challenges of lithium metal anode are still considerable [103]. Previous researches on the anode side mainly focused on the stability of SSEs with lithium, the ion migration on the interface of SSEs and lithium, and the even deposition of lithium [104–107]. The high density nuclearation and unifom plating of Li metal are highly concerned [108–110]. It is worth noting that these three aspects are correlative and codetermine the compatibility between SSEs and lithium metal.

Tatsumisago and co-workers [111] found that the impedance of resting Li/$80Li_2S{\cdot}20P_2S_5$/Li symmetric cell initially increased and then became stable over time. Yamada *et al.* [76] found similar phenomenon while investigating Li_3PS_4. They attributed the initial impedance increase to the reaction between SSEs and lithium metal. A stable interphase was considered being formed and preventing further reaction, which ensured the stability between SSEs and lithium metal.

However, above-mentioned stability may be not suitable for the batteries during charge and discharge. The deposition state of lithium, the distribution of stable interface, and the diffusion of ions and electrons are also needed to be considered. Dendrites might destroy the incompact interphase so that the interphase could not play an effective role in preventing the reaction between SSEs and lithium metal.

Yamada *et al*. [76] compared the electrochemical impedance spectroscopy (EIS) of Li/Li symmetric cell using Li_3PS_4 with that of the Li/Li symmetric cell using conventional OLEs. It was found that while using conventional OLEs, the charge transfer resistance (R_{ct}) had very little change after the stripping-deposition of lithium. However, the R_{ct} of Li/Li symmetric cell using Li_3PS_4 decreased a lot after the same treatment. They then calculated the exchange current density i_0 of these two kinds of symmetric cells before and after the stripping-deposition of lithium at different temperatures. The activation energy of ion migration was further obtained based on the i_0. Consistent with the R_{ct}, the activation energy of symmetric cell using OLEs changed very little (from 68.4 to 67.6 kJ mol^{-1}) after the stripping-deposition of lithium, but the activation energy of symmetric cell using Li_3PS_4 decreased a lot (from 52.1 to 44.5 kJ mol^{-1}). Following explanation was given by Yamada *et al*. [76]: employing solid electrolyte, the original solid electrolyte interphase (SEI) on the surface of lithium was destroyed during the stripping-deposition and the lithium directly contacted the solid electrolyte, which led to the significant reduction of activation energy. In the liquid electrolyte, an additional organic SEI was formed after the original SEI being destroyed [112,113], so the activation energy changed little. Although Yamada *et al*. ignored the reaction between Li_3PS_4 and lithium, there is no denying that the stable interphase between lithium and solid electrolyte would be destroyed under uncontrolled stripping-deposition of lithium. It might somehow reduce the resistance of ion migration, but such an unstable interface would intensify the uneven deposition of lithium and cause the continuous dissipation of both electrolyte and lithium anode.

Sufficient and effective interfacial contact between SSEs and lithium metal was beneficial to the uniform deposition of lithium and extraordinary stability. Nagao *et al.* [114] covered a lithium thin film on the surface of $80Li_2S$-$20P_2S_5$ pellet through vacuum evaporation (Figure 7(d)). The Li/Li symmetric cell with such modified $80Li_2S$-$20P_2S_5$ pellet electrolyte was very stable during galvanostatic cycles. In comparison, the voltage of Li/Li symmetric cell with a conventional $80Li_2S$-$20P_2S_5$ pellet electrolyte significantly varied during cycles (Figure 7(e, f)), which is originated from the unstable interfaces.

Besides employed in all-solid-state Li-S batteries, SSEs also exhibited the potential of fabricating functional interphases to stabilize the lithium anode in routine Li-S batteries

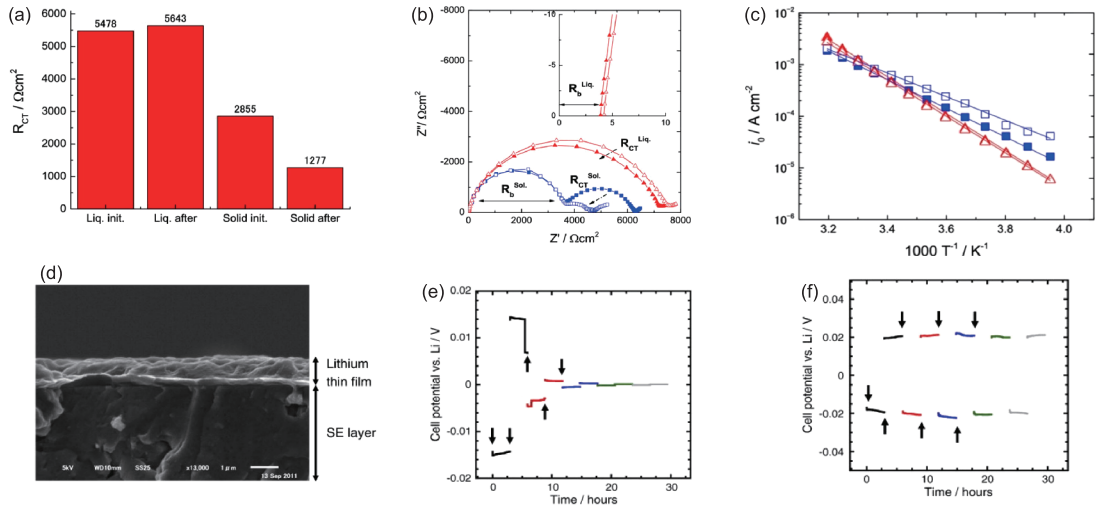

Figure 7 Li_3PS_4 solid electrolyte cells. (a) R_{ct} for both liquid and Li_3PS_4 solid electrolyte cells before and after the stripping-deposition cycles. (b) EIS of solid (blue) and liquid (red) electrolyte symmetrical Li/Li cells at −20 °C. (c) Temperature dependence of the exchange current density i_0 for a Li/Li^+ redox couple in the Li_3PS_4 solid (blue squares) and the liquid (red triangles) electrolytes. The solid and open symbols refer to i_0 before and after a galvanostatic stripping-deposition cycle, respectively. Reprinted with permission from Ref. [76], copyright 2015, The Electrochemical Society. (d) SEM image of cross-section of the solid electrolyte (SE) layer with a lithium thin film. Galvanostatic charge-discharge curves of Li/Li symmetric cells with (e) unmodified solid electrolyte and (f) thin lithium coated solid electrolyte. Reprinted with permission from Ref. [114], copyright 2012, Elsevier (color online).

with OLEs. Recently, our group [115,116] reported a kind of sulfurized SEI. Compared with routine SEI, sulfurized SEI attached on Li metal anode renders a very high ionic conductivity [117]. The ion pathways in sulfurized SEI were uniform and very abundant, which is beneficial to the even stripping-deposition of lithium. This significantly enhances the cycle performance of lithium metal anode. The coulombic efficiency of Li/Cu coin cell with sulfurized SEI was around 98% after 200 cycles under 1.0 mA cm^{-2} [118]. The regulation of the composition of SEI is a prospective way to stabilize the interface and guide the even stripping-deposition of lithium, which is crucial for both all-solid-state Li-S batteries and conventional Li-S batteries with OLEs.

3 Oxide solid electrolyte

Oxide solid electrolyte is another large family in the ionic materials with rapid ion diffusion channels. The oxide solid electrolyte has been strongly considered for solid state Li metal batteries. This section summarized three types of oxide solid electrolyte in the following: perovskite-type, NASICON-type and garnet-type to focus on their application in Li-S batteries.

3.1 Introduction of oxide solid electrolyte

3.1.1 Perovskite-type

The general formula of ideal perovskite structure is ABO_3. It owns cubic unit cell and belongs to space group $Pm\bar{3}m$. A ions, B ions, and oxygen anions locate at the corners, body-centers, and face-centers of the cube respectively. A sites and B sites are in 12-fold coordination (AO_{12}) and 6-fold coordination (BO_6) respectively. AO_{12} and BO_6 share corners with each other. Through aliovalent doping, lithium ions are able to be introduced in the A sites of perovskite structure. At the same time, A-site deficient structure (e.g. $Li_{3x}La_{2/3-x}\square_{1/3-2x}TiO_3$) is formed. It is obvious that the concentrations of both lithium and vacancy are raised [119], which significantly increases the ionic conductivity. In A-deficient perovskite structure, Li^+ can diffuse by jumping to adjacent vacancy in the *ab* plane through a square planar bottleneck formed by the oxygen on the corners of BO_6 (Figure 8(a)) [120]. The introduction of large size ions, such as rare-earth metal ions and alkaline-earth metal ions, is an efficient method to increase the bottleneck size and accelerate the Li^+ migration. As increasing the size of rare-earth metal ions ($Sm^{3+}<Nd^{3+}<Pr^{3+}<La^{3+}$), higher ionic conductivity and lower activation energy are achieved [121]. $Li_{0.34}La_{0.56}TiO_3$ exhibits the highest ionic conductivity of 10^{-3} S cm^{-1} at room temperature in the family of perovskite materials. Besides of the size of bottleneck, the interaction between B-site cation and coordinated oxygen anion also affects the ionic conductivity. Weakening their bond strength increases the ionic conductivity. However, it is only suitable for a narrow concentration range of Ti^{4+} substitution by Al^{3+} and display little practical value [122].

3.1.2 NASICON-type

The general formula of NASICON-type lithium ion conductor is $Li_{1+6x}M^{4+}{}_{2-x}M'^{3+}{}_x(PO_4)_3$ (M=Ti, Ge, Sn, Hf, or Zr and M′=Cr, Al, Ga, Sc, Y, In, or La). Most of them have a rhombohedral unit cell and belong to space group $R\bar{3}m$. Several monoclinic and orthorhombic phases have been reported [123,124]. There are two different Li-sites (M1 and M2) in

the structure. The M1 sites locate between two MO_6 octahedra directly and are 6-fold coordinated. The M2 sites locate two columns of MO_6 octahedras and are 8-fold coordinated. These Li-sites are partially occupied by Li^+ and the Li^+ migration in NASICON structure is achieved by Li^+ hopping between M1 sites and M2 sites. Additionally, vacancies at the interaction of above-mentioned Li^+ pathway are requested to fabricate the three-dimensional pathway for Li^+ (Figure 8(b)) [125–127]. To increase the ionic conductivity of NASICON-type lithium ion conductor, there are two main strategies. Firstly, increasing the size of the network, especially the bottleneck size, is able to significantly raise the ionic conductivity. It was found that the activation energy of Li^+ migration decreased linearly with the increase of bottleneck size between the M1 and M2 sites. Using larger M cation is able to expand the bottleneck and increase the ionic conductivity. For example, replacing the Ge^{4+} (0.53 Å) and Ti^{4+} (0.605 Å) in $LiMM'(PO_4)_3$ with Hf^{4+} (0.71 Å) is able to increase the ionic conductivity up to 4 orders of magnitude [128]. Secondly, substituting the M'^{4+} with M'^{3+}, such as Al^{3+} and Sc^{3+}, is an effective way to increase the ionic conductivity. Such aliovalent substitution is able to increase the concentration and mobility of Li^+. However, the substitution level is limited to 15% because of the huge radius mismatch. A secondary phase is formed while going beyond this level [129]. Besides high ionic conductivity, another advantage of NASICON-type lithium ion conductors is their high stability. They are stable with air and water. Their electrochemical stability at high potential is also excellent [130], which is beneficial to their practical applications in high power density battery systems.

3.1.3 Garnet-type

The general formula of garnet structure is $A_3B_2(XO_4)_3$. It owns cube unit cell and belongs to space group $1a\bar{3}d$. A cations locate in 8-fold coordinated antiprismatic sites, and B cations locate in 6-fold coordinated octahedral sites. Conventionally, the lithium ions in garnet-type ion conductor occupy the tetrahedral positions. More lithium ions are able to be introduced through adjusting the valence of A and B cations. For instance, replacing La^{3+} with divalent cations and M with Zr^{4+} in $Li_5La_3M_2O_{12}$ is able to obtain higher lithium ion concentrations. These extra lithium ions occupy other sites besides tetrahedral positions, such as distorted octahedral positions (Figure 8(c)). Normally, it was thought that higher Li^+ concentration leads to the faster lithium-ion conduction. However, the aliovalent substitution regulates the distribution of lithium ions in the tetrahedral and distorted octahedral positions [131,132], which is another reason for the rise of ionic conductivity. For instance, the ionic conductivity increases by nine orders of magnitude from $Li_3Ln_3Te_2O_{12}$ to $Li_7La_3M_2O_{12}$ [112]. Such huge improvements were ascribed to not only the increase of lithium ion concentration, also the lithium ions occupying the distorted octahedral positions, which accelerated the ion migration rate and leads to higher ionic conductivity. Additionally, cubic structure was crucial to achieve high ionic conductivities for certain garnet-type lithium ion conductors. The $Li_7La_3Zr_2O_{12}$ (LLZO) is a kind of garnet-type lithium ion conductor and has been widely used in the research of solid state batteries. Undoped LLZO owns tetragonal structure. Aluminum doping is able to stabilize LLZO in the cubic form and enhance the ionic conductivity by two orders of magnitude [133]. Additionally, the formation of $LiAlSiO_4$ and $LiGaO_2$ at the grain boundary also contributed to the high ionic conductivities of Al-doped LLZO [134] and Ga-substituted LLZO [135].

Furthermore, garnet-type lithium ion conductors render high thermal stabilities up to 900 °C. They are also stable when contacting lithium metal, which makes them a good candidate of solid electrolyte in lithium metal batteries [136].

3.2 The application in Li-S batteries with hybrid electrolyte

Unlike SSEs, OSEs exhibit high hardness and poor interface contact with electrodes. High temperature (>1000 K) annealing is indispensable to reducing interfacial resistance and achieving considerable ionic conductivity. However, sulfur cathode cannot bare such a high temperature. Consequently, it is unpractical to make all-solid-state Li-S batteries with OSEs only. OSEs were widely applied to fabricate hybrid electrolytes for Li-S batteries.

Wen and co-workers [137] firstly exploited an inorganic solid electrolyte, $Li_{1.5}Al_{0.5}Ge_{1.5}(PO_4)_3$ (LAGP), as an interlayer for fabricating a Li-S battery with hybrid electrolyte, lithium metal as anode and Ketjen black-sulfur composition as cathode (Figure 9(a)). The 1.0 M $LiN(CF_3SO_2)_2$ (LiTFSI) in 1,3-dioxolane (DOL) and 1,2-dimethoxyethane (DME) (1:1, *v*/*v*) organic liquid electrolyte was applied to connect the electrode and the solid electrolyte interlayer. The as-prepared hybrid electrolyte Li-S batteries exhibited initial discharge capacities of up to 1528, 1386, and 1341 mA h g^{-1} at C/20, C/5, and C/2 respectively (Figure 9(b)). In comparison, initial discharge capacities of liquid electrolyte Li-S batteries reach merely 719, 578, and 467 mA h g^{-1} respectively at the same rate (Figure 9(c)). Additionally, there were obvious overcharge in the liquid electrolyte Li-S batteries due to the shuttle effect. Figure 9(d) exhibits the cycle performances of hybrid electrolyte Li-S battery and liquid electrolyte Li-S battery. The reversible capacity remained at 720 mA h g^{-1} after 40 cycles at C/5 for Li-S batteries with hybrid electrolytes. An excellent columbic efficiency of around 100% was achieved. The solid electrolyte interlayer effectively hindered the diffusion of polysulfides and the shuttle effects were therefore eliminated. Recently, Yu *et al.* [138] applied another NASICON-type lithium ion conductor,

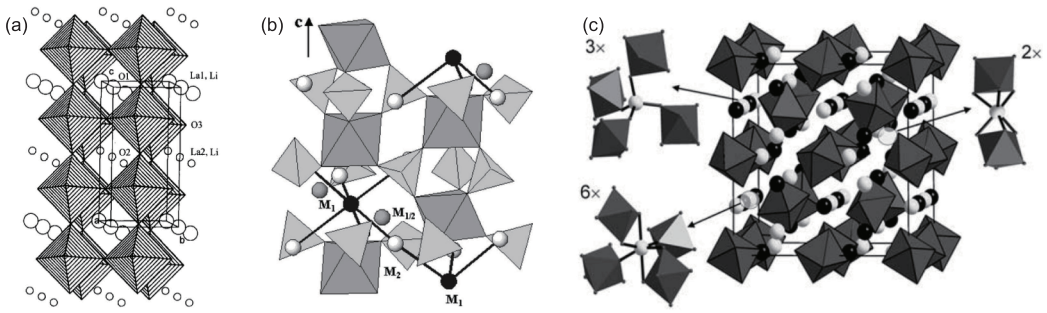

Figure 8 (a) Crystal structure of $Li_{3x}La_{2/3-x}\square_{1/3-2x}TiO_3$ (○=La, Li or vacancies in position (0, 0, 0); ○=La, Li or vacancies in position (0, 0, ½); lines represent the unit cell).. Reprinted with permission from Ref. [120], copyright 1996, Elsevier. (b) Rhombohedral structure of NASICON materials in which M_1, $M_{1/2}$, and M_2 sites are susceptible to be occupied by lithium. Reprinted with permission from Ref. [126], copyright 2005, American Physical Society. (c) The crystal structure of a conventional garnet $A_3B_3C_2O_{12}$ where octahedra indicate CO_6 units and black and grey spheres represent A and B cations respectively. In addition to the three C sites occupied in conventional garnets, suitable sites for lithium cations in $Li_5La_3M_2O_{12}$ include the six octahedral and two trigonal prismatic sites indicated. 18 selected positions for these two additional coordination sites are indicated by transparent spheres within the garnet unit cell. Reprinted with permission from Ref. [132], copyright 2010, Royal Society of Chemistry.

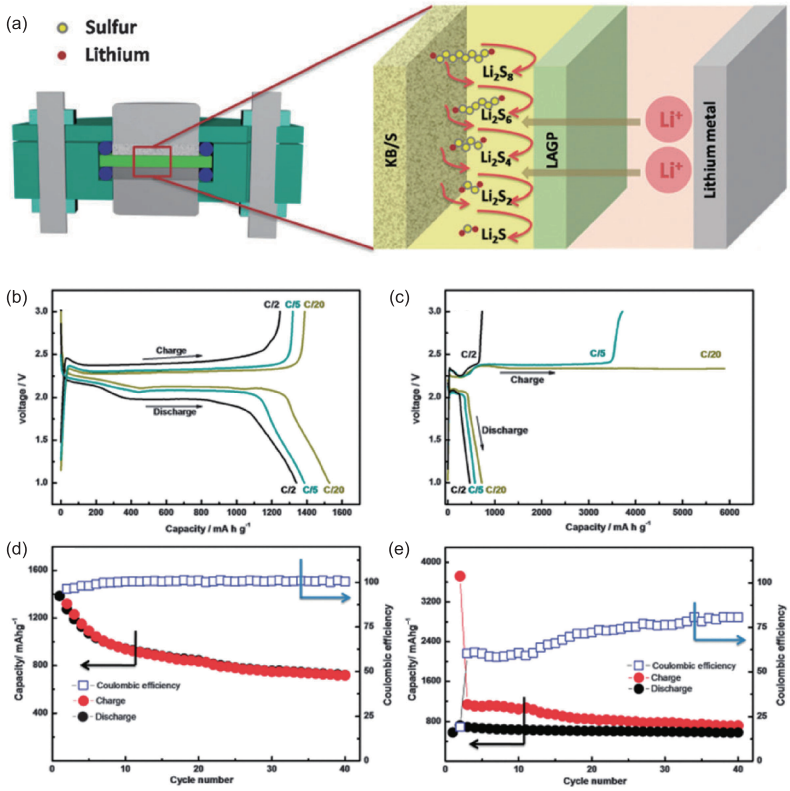

Figure 9 The Li-S cell with hybrid electrolytes. (a) Schematic illustration. Voltage versus specific charge-discharge capacity profiles of initial galvanostatic cycles of Li-S cells with (b) hybrid electrolyte and (c) liquid electrolyte at C/2, C/5 and C/20 rates. Cycling performance and coulombic efficiency of Li-S cells with (d) hybrid electrolyte and (e) liquid electrolyte. Reprinted with permission from Ref. [137], copyright 2014, Royal Society of Chemistry (color online).

$Li_{1+x}Y_xZr_{2-x}(PO_4)_3$ (LYZP), as a solid-electrolyte/separator to suppress polysulfide-crossover in Li-S batteries. LYZP exhibited both favorable chemical compatibility with lithium sulfides and excellent electrochemical stability under the operating condition. The hybrid electrolyte Li-S batteries were prepared with a lithium-foil anode and a dissolved polysulfide (Li_2S_6) cathode (named as catholyte). The LYZP membrane was introduced to separate the lithium anode and the polysulfide catholyte. A piece of polypropylene (PP) thin film was inserted between LYZP membrane and lithium anode to build up a facile ionic interface. The hybrid electrolyte Li-S batteries developed in this work delivered an initial discharge capacity of ~1000 mA h g^{-1} (based on the active sulfur material) and retained ~90% of the initial capacity after 150 cycles at a rate of 0.2 C. Judez *et al.* [139] fabricated of polymer-rich PEO/lithium bis(fluorosulfonyl)imide composite electrolytes containing either Li-ion conducting glass ceramic or inorganic Al_2O_3 were applied as hybrid electrolyte for Li-S cells.

The cells with Al_2O_3 additive working at 70 °C exhibited a discharge capacity of 518 mA h g^{-1} and 0.53 mA h cm^{-2} with a Coulombic efficiency of more than 99% at the end of 50 cycles. A mixture of carbon black, metal organic framework (MIL-53(Al)), PEO, and LiTFSI are employed as an interlayer with electronic conductor and solid polymer electrolyte between cathode and electrolyte in a solid state Li-S batterie [140]. The as-obtained cell at 80 °C exhibited have a high capacity of 792.8 mA h g^{-1} after 50 cycles at 0.5 C.

The hybrid electrolyte with liquid electrolyte has the risk of leakage and evaporation. Replacing liquid electrolyte with polymer is an effective strategy to overcome this issue. Wen and co-workers [141] designed a facile gel-ceramic multi-layer electrolyte for Li-S batteries. The multi-layer electrolyte was composite of a LAGP ceramic layer and a poly(ethylene oxide) (PEO) based gel-polymer electrolyte (GPE) (gel-forming liquid electrolyte 1 M LiTFSI TEGDME) (Figure 10(a)). The LAGP solid electrolyte was employed to block the polysulfides on the cathode side and control the shuttle effect. The PEO-based GPE provided sufficient flexibility to maintain a low interfacial resistance. At the same time, this avoided the leakage and evaporation of electrolyte. The LAGP and the GPE are stuck well (Figure 10(b, c)), which provides the access to the fast ion migration on the interface. The commercial carbon paper kept porous when filled with GPE, which made it possible to further improve the liquid uptake. The Nyquist plot was composed of two partially overlapped semicircles in high and medium frequency regions, and a straight slopping line in low frequency region (Figure 10(d)). The semicircle in high frequency region was probably derived from the interfacial contact resistance between the gel electrolyte and the solid electrolyte. The semicircle at medium frequency region corresponded to the charge transfer resistance. The inclined straight line in low frequency region reflected the lithium ion diffusion within the electrode. With the gel-ceramic multi-layer electrolyte, an excellent battery performance with high capacity, high coulombic efficiency and good cycling stability was achieved. Initial discharge capacities of 1376, 1249, 1058, and 725 mA h g^{-1} were obtained at the rate of C/20, C/10, C/5, and C/2, respectively (Figure 10(e)). The specific capacity remained at 700 mA h g^{-1} after 300 cycles at C/2.

Recently, Cui and co-workers [142] reported a facile synthesis of Al^{3+}/Nb^{3+} co-doped cubic LLZO nanoparticles and LLZO nanoparticle-decorated porous carbon foam (LLZO@C) by the one-step Pechini sol-gel method. The LLZO nanoparticles were added into PEO to fabricate hybrid electrolyte (Figure 11(a)). Compared with filler-free samples, the LLZO nanoparticle-filled PEO electrolyte (LLZO-PEO-$LiClO_4$) exhibited high ionic conductivity. Through adjusting the concentration of LLZO nanoparticles in PEO, the highest ionic conductivities of 9.5×10^{-6} and 1.1×10^{-4} S cm^{-1} were obtained at 20 and 40 °C respectively (Figure 11(b)). The solid-state Li-S battery with LLZO-PEO-$LiClO_4$ as electrolyte, S@LLZO@C as cathode, and lithium metal as anode delivers an attractive specific capacity of over 900 mA h g^{-1} based on the mass of sulfur at 37 °C, which is much higher than routine C@S cathode (Figure 11(c, d)). Figure 11(e) exhibited the cycling performance of as-prepared solid-state Li-S batteries. The capacity decay mainly took place in the initial several cycles and the capacity retention was able to reach as high as 98.7% after 90 cycles compared to the 10th cycle. Besides, the coulombic efficiency approached ~100% during the cycling, although the corresponding coulombic efficiencies for the initial several cycles were higher than 100%, which was attributed to the irreversible electrochemical reaction of Li_2S. The excellent electrochemical performance resulted from the rational design of the composition cathode and solid electrolyte, in which the LLZO nanoparticles performed as both the filler to improve the ionic conductivity and the interfacial stabilizer to reduce the interfacial resistance. Recently, Tao and co-workers [143] further described the exploration of poly(ethylene oxide) based solid-state polymer electrolytes containing ionic liquid grafted ZrO_2, TiO_2, and SiO_2 nanoparticles for Li-S batteries. The ionic liquid grafted ZrO_2 system exhibited the largest ionic conductivity of 2.32×10^{-4} S cm^{-1} at 37 °C, which affords a Li-S battery with the hybrid electrolyte a high specific capacity of 986 and 600 mA h g^{-1} at 50 and 37 °C, respectively.

Very recently, Hu and coworkers [144] demonstrated in lithium sulfur battery system a three-dimensional bilayer garnet type LLZO solid-state electrolyte, which composed of a thin dense layer and a thick porous layer. The dense layer avoided the penetration of lithium metal, enabling the safety of the anode. The thick porous layer acted simultaneously as a mechanical support for the thin dense LLZO, and as a 3D host for sulfur cathode materials, providing pathways for continuous ion transfer. This structure effectively eliminated shuttle effect in lithium sulfur cells and contributed to an high coulombic efficiency above 99%. The 3D solid electrolyte also enabled the high areal loading of sulfur into the porous layer. An intermediary Li-Al alloy that regulates the lithiophobic to lithiophilic garnet surface and reduces the resistance at interfaces is verified and applied in solid Li-S batteries [145]. An initial discharge capacity of 1532 mA h g^{-1} and a 90.6% coulombic efficiency are achieved. Both very high discharge capacity and >99% coulombic efficiency are obtained based on the garnet effectively blocks the shuttle of polysulfides in working Li-S batteries. This work shed some lights on the smart-designed interface between OSEs and sulfur cathodes. Zhang and co-workers [146] described a flexible anion-immobilized PEO-LiTFSI-LLZTO composite

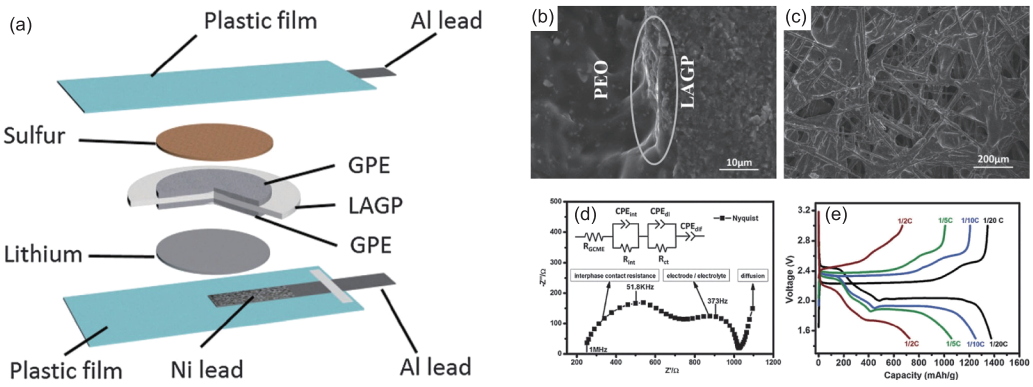

Figure 10 Li-S cell with gel-ceramic multi-layer electrolyte. (a) Schematic illustration; (b) SEM image of the cross section of the gel-ceramic multi-layer electrolyte; (c) SEM image of porous carbon paper soaked with the gel-polymer electrolyte; (d) Nyquist plot of the Li-S cell at the fully charged state and the inset shows the proposed equivalent circuit for the Li-S cell; (e) initial discharge/charge profiles at C/20, C/10, C/5 and C/2 rates. Reprinted with permission from Ref. [141], copyright 2016, Royal Society of Chemistry (color online).

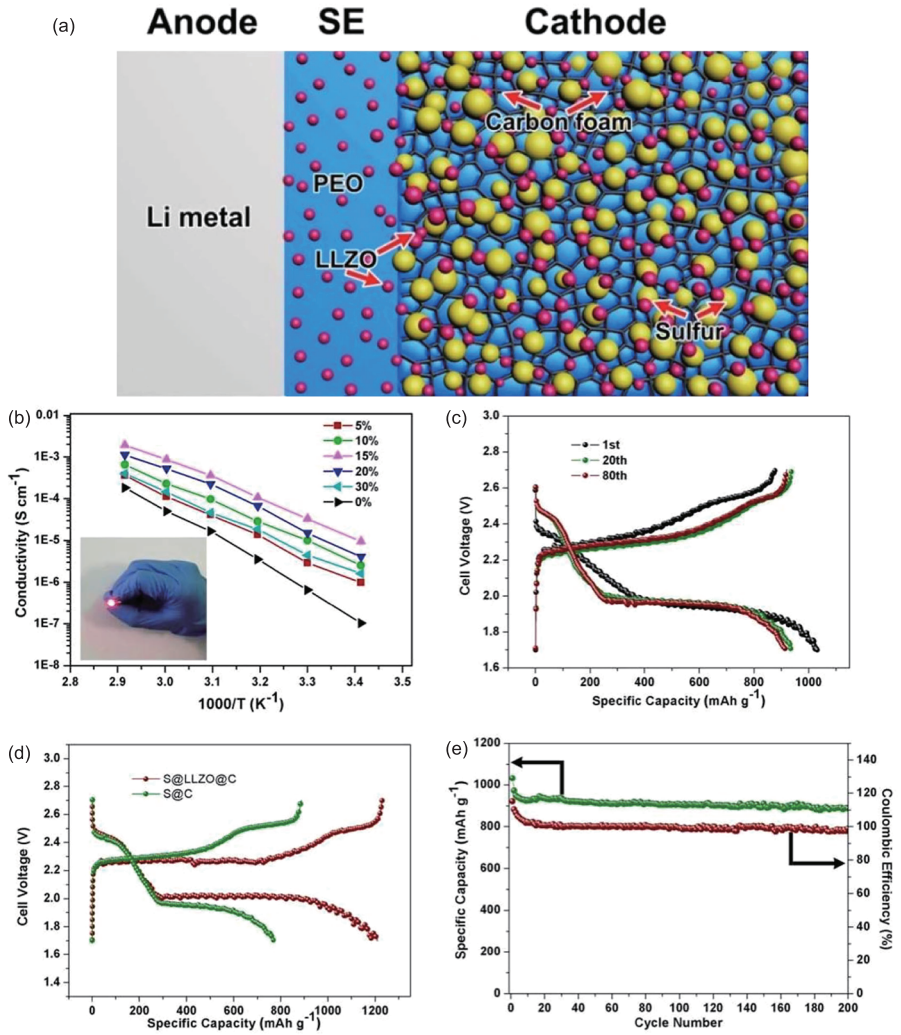

Figure 11 All solid-state Li-S battery based on LLZO electrolyte. (a) Schematic illustration. (b) Arrhenius plots of the conductivity of nanocomposite LLZO-PEO-$LiClO_4$ with different LLZO concentrations. The inset is an optical photograph of a red LED lightened by the solid-state Li-S batteries between the fingers. (c) Typical charge/discharge curves of the first, 20th, and 80th cycles of the S@LLZO@C cathode with a current density of 0.05 mA cm^{-2} at 37 °C. (d) Typical charge/discharge curves of the S@LLZO@C and S@C cathodes with of 0.1 mA cm^{-2} at 50 °C. (e) Cycling performance and Coulombic efficiency of the S@LLZO@C cathode with a current density of 0.05 mA cm^{-2} at 37 °C. Reprinted with permission from Ref. [142], copyright 2017, American Chemical Society (color online).

electrolyte to inhibit Li dendrites and construct safe all solid state rechargeable batteries. The exploration of an anion-immobilized composite solid state electrolyte renders a promising opportunity for next-generation safe and flexible Li-S batteries [147,148].

Furthermore, multi-functional layers which were composed of solid electrolytes and conductive carbon materials were investigated in several recent works. Jin *et al.* [149] explored a mixed conductive coating layer composed of LAGP, Super P, and polyvinylidene fluoride (PVDF) and introduced it on the surface of a sulfur electrode. This coating layer was desired to suppress the diffusion of polysulfides and achieve the efficient utilization of active materials at the same time. The protected sulfur cathode delivered an initial specific capacity of 1236 mA h g^{-1} at 0.5 C and maintained a capacity of 842 mA h g^{-1} after 100 cycles which was about 200 mA h g^{-1} higher than the pristine cathode without mixed conductive coating. The rate performance of the protected cathode in a soft package battery was also tested. A specific capacity of 982.2, 931.2, and 758.7 mA h g^{-1} were obtained at the current densities of 1.0, 2.0, and 5.0 A g^{-1} respectively. Even at 10 A g^{-1}, a specific capacity of 355 mA h g^{-1} was achieved, which was an ultrahigh rate performance for soft package Li-S batteries. Wen and co-workers [150] further described an interface modified hybrid electrolyte. A carbon coating layer facing sulfur cathode was introduced on one side of solid electrolyte LAGP (Figure 12(a)). This carbon coating was composed of acetylene black and carbon nanotube (CNT) at the ratio of 3:1 (*w*/*w*) and was about 5 μm thick on average (Figure 12(b)). The carbon coating layer exhibited a much lower contact angle than the uncoated solid electrolyte (Figure 12(c, d)). The improved wettability was beneficial to the conversion of the dissolved polysulfides at the three-phase boundary between carbon, sulfur, and electrolyte. Much higher capacities and significantly improved cycling stability are achieved for the Li-S batteries with the carbon coated solid electrolyte due to the facilitated conversion of redox reaction. The Li-S batteries containing carbon coated solid electrolyte delivered an initial specific capacity of 1409 mA h g^{-1} and remained at 1000 mA h g^{-1} after 50 cycles at the rate of 0.2 C, which were much higher than those of the Li-S batteries with pristine solid electrolyte

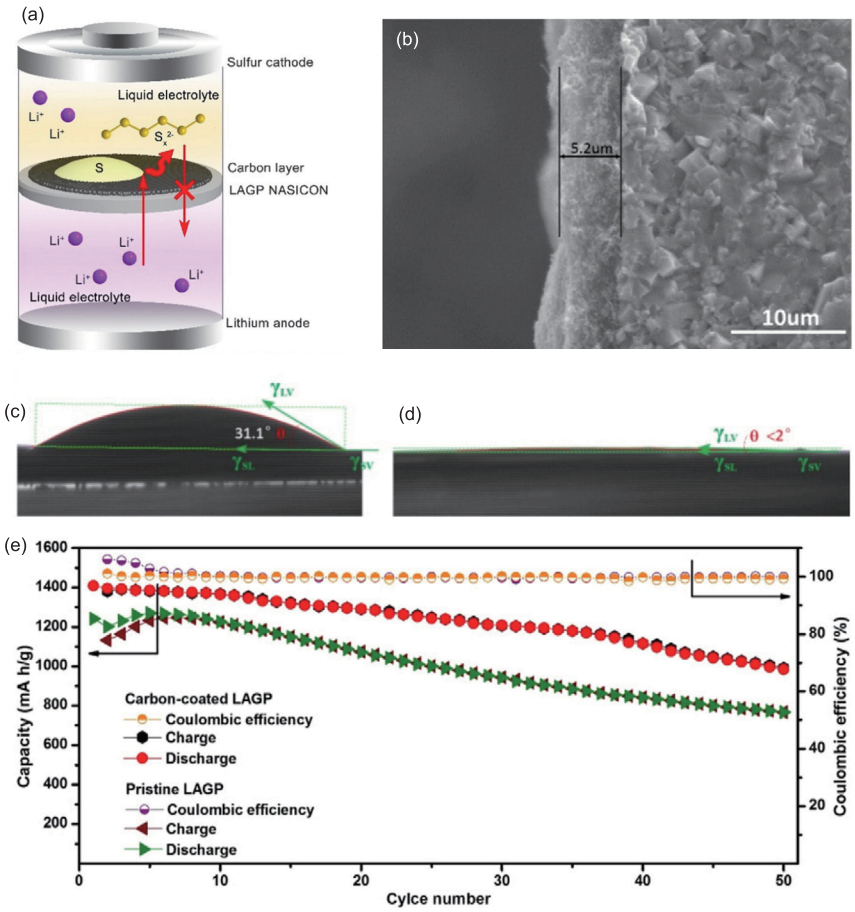

Figure 12 Li-S battery configuration with a carbon-coated LAGP electrolyte. (a) Schematic illustration. (b) SEM image of the cross section of the carbon-coated LAGP. Contact angle snapshots for Li_2S_8/tetraethyleneglycol dimethylether (TEGDME) on (c) pristine LAGP and (d) carbon-coated LAGP. (e) Cycling performance of the Li-S cells. Reprinted with permission from Ref. [150], copyright 2017, Elsevier (color online).

(Figure 12(e)). Additionally, it is worth noting that both batteries exhibited superb coulombic efficiencies of approaching 100% because the shuttle effect was totally suppressed in these hybrid electrolyte Li-S batteries.

4 Conclusions and perspective

The inorganic solid electrolytes play an important role in safe Li-S batteries. In particular, SSEs and OSEs are applied in different ways due to their different physical and electrochemical properties.

For SSEs, they are mainly applied in all-solid-state Li-S batteries, which renders them face the challenges from both cathode side and anode side. On the cathode side, the poor electrical and ionic conductivities of S and Li_2S become more serious due to the immobility of solid electrolyte and the absence of soluble redox intermediates. It is crucial to fabricate an efficient electron and ion pathway inside the cathode. To achieve this target, previous researches mainly focused on the following strategies: Firstly, nanocrystallized and nanostructured frameworks were used to increase the contact area among active materials, solid electrolytes, and conductive additives. Secondly, the interfacial condition of active materials and solid electrolyte was optimized via *in-situ* reaction, *ex-situ* interface modification etc. Consequently, the interfacial migration rate was raised. Thirdly, novel active materials with considerable ionic conductivities were able to be synthesized through the complex reactions between sulfur and SSEs, which might solve the problem essentially. On the anode side, the interfacial compatibility between SSEs and lithium metal is the core issue. The interfacial ion migration and the stripping-deposition state of lithium are also considerable. The incorporation of well-designed interface layer between SSEs and lithium metal anode affords the feasibility towards the compatible SSEs into lithium metal batteries.

For OSEs, they are mainly applied to fabricate hybrid electrolyte for Li-S batteries. The interfacial contact between OSEs and electrodes can be significantly enhanced by the incorporation of OSEs with polymer or liquid electrolyte. The OSEs always played a critical role of hindering the migration of polysulfides and regulating the shuttle of intermediates in working Li-S batteries. Combining OSEs layer with carbon materials was also explored to promote the redox transition of Li-S reaction.

In spite of above research progresses, there are large open space remained to be exploited in the field of ISEs for Li-S batteries. For instance, it is a grand challenge to fabricate effective ion-electron hybrid conduction pathways for the composite cathode of all-solid-state Li-S batteries. It is rewarding to carry out further investigations on the reactions between sulfur and SSEs from the viewpoint of chemistry and materials science. On the anode side, the rational physical or chemical modification on the surface of SSEs is strongly considered to improve the compatibility between SSEs and lithium metal. In addition, considering that lots of OSEs are stable with lithium metal, hybrid electrolytes with SSEs on the cathode side and OSEs on the anode sides will be suitable for all-solid-state Li-S batteries.

At present, the practical applications of ISEs for Li-S batteries are staying at the early stage of the scientific research and engineering development. There are numerous challenges and opportunities in this research field. More fundamental understandings on the materials and energy chemistry are crucial for further rational design of solid state electrolyte for safe Li-S batteries.

Acknowledgments This work was supported by the National Key Research and Development Program (2016YFA0202500, 2015CB932500) and the National Natural Science Foundation of China (21676160, 21776019). We thank X.B. Cheng, X.Q. Zhang, R. Xu, H.J. Peng, and P.Y. Chen for helpful discussion.

Conflict of interest The authors declare that they have no conflict of interest.

1 Armand M, Tarascon JM. *Nature*, 2008, 451: 652–657
2 Dunn B, Kamath H, Tarascon JM. *Science*, 2011, 334: 928–935
3 Rosenman A, Markevich E, Salitra G, Aurbach D, Garsuch A, Chesneau FF. *Adv Energ Mater*, 2015, 5: 1500212
4 Tu Y, Deng D, Bao X. *J Energ Chem*, 2016, 25: 957–966
5 Hu H, Guan BY, Lou XWD. *Chem*, 2016, 1: 102–113
6 Li D, Zhang Y, Li L, Hu F, Yang H, Wang C, Wang Q. *Sci China Chem*, 2016, 59: 122–127
7 Goodenough JB. *Energ Storage Mater*, 2015, 1: 158–161
8 Nitta N, Wu F, Lee JT, Yushin G. *Mater Today*, 2015, 18: 252–264
9 Chen R, Luo R, Huang Y, Wu F, Li L. *Adv Sci*, 2016, 3: 1600051
10 Zhang X, Cheng X, Zhang Q. *J Energ Chem*, 2016, 25: 967–984
11 Li W, Zeng L, Wu Y, Yu Y. *Sci China Mater*, 2016, 59: 287–321
12 Xiong J, Han C, Li Z, Dou S. *Sci Bull*, 2015, 60: 2083–2090
13 Yin YX, Xin S, Guo YG, Wan LJ. *Angew Chem Int Ed*, 2013, 52: 13186–13200
14 Peng HJ, Huang JQ, Zhang Q. *Chem Soc Rev*, 2017, 46: 5237–5288
15 Fang R, Zhao S, Sun Z, Wang DW, Cheng HM, Li F. *Adv Mater*, 2017, 451: 1606823
16 Manthiram A, Chung SH, Zu C. *Adv Mater*, 2015, 27: 1980–2006
17 Imtiaz S, Zhang J, Zafar ZA, Ji S, Huang T, Anderson JA, Zhang Z, Huang Y. *Sci China Mater*, 2016, 59: 389–407
18 Zhou K, Fan XJ, Wei XF, Liu JH. *Sci China Tech Sci*, 2017, 60: 175–185
19 Peng HJ, Huang JQ, Cheng XB, Zhang Q. *Adv Energ Mater*, 2017, 451: 1700260
20 Cheng XB, Zhang R, Zhao CZ, Zhang Q. *Chem Rev*, 2017, 117: 10403–10473
21 Manthiram A, Fu Y, Chung SH, Zu C, Su YS. *Chem Rev*, 2014, 114: 11751–11787
22 Seh ZW, Sun Y, Zhang Q, Cui Y. *Chem Soc Rev*, 2016, 45: 5605–5634
23 Liang J, Sun ZH, Li F, Cheng HM. *Energ Storage Mater*, 2016, 2: 76–106
24 Lin Z, Liang C. *J Mater Chem A*, 2015, 3: 936–958
25 Peng HJ, Xu WT, Zhu L, Wang DW, Huang JQ, Cheng XB, Yuan Z, Wei F, Zhang Q. *Adv Funct Mater*, 2016, 26: 6351–6358

26 Huang JQ, Zhang Q, Wei F. *Energ Storage Mater*, 2015, 1: 127–145
27 Peng HJ, Wang DW, Huang JQ, Cheng XB, Yuan Z, Wei F, Zhang Q. *Adv Sci*, 2016, 3: 1500268
28 Zhuang TZ, Huang JQ, Peng HJ, He LY, Cheng XB, Chen CM, Zhang Q. *Small*, 2016, 12: 381–389
29 Peng HJ, Zhang ZW, Huang JQ, Zhang G, Xie J, Xu WT, Shi JL, Chen X, Cheng XB, Zhang Q. *Adv Mater*, 2016, 28: 9551–9558
30 Goodenough JB, Kim Y. *Chem Mater*, 2010, 22: 587–603
31 Xu K. *Chem Rev*, 2004, 104: 4303–4418
32 Gao J, Ren W, Chen J. *Energy Storage Sci Technol*, 2017, 6: 557–571
33 Sun Y, Huang J, Zhang X, Zhang Q. *Energy Storage Sci Technol*, 2017, 6: 464–478
34 Xin S, You Y, Wang S, Gao HC, Yin YX, Guo YG. *ACS Energ Lett*, 2017, 2: 1385–1394
35 Bachman JC, Muy S, Grimaud A, Chang HH, Pour N, Lux SF, Paschos O, Maglia F, Lupart S, Lamp P, Giordano L, Shao-Horn Y. *Chem Rev*, 2016, 116: 140–162
36 Xiayin Y, Bingxin H, Jingyun Y, Gang P, Zhen H, Chao G, Deng L, Xiaoxiong X. *Chin Phys B*, 2016, 25: 018802
37 Varzi A, Raccichini R, Passerini S, Scrosati B. *J Mater Chem A*, 2016, 4: 17251–17259
38 Chen R, Qu W, Guo X, Li L, Wu F. *Mater Horiz*, 2016, 3: 487–516
39 Yue L, Ma J, Zhang J, Zhao J, Dong S, Liu Z, Cui G, Chen L. *Energ Storage Mater*, 2016, 5: 139–164
40 Liu D, Zhu W, Feng Z, Guerfi A, Vijh A, Zaghib K. *Mater Sci Eng-B*, 2016, 213: 169–176
41 Sakuda A, Hayashi A, Tatsumisago M. *Sci Rep*, 2013, 3: 2261
42 Mizuno F, Hayashi A, Tadanaga K, Tatsumisago M. *Adv Mater*, 2005, 17: 918–921
43 Tatsumisago M. *Solid State Ion*, 2004, 175: 13–18
44 Hayashi A, Hama S, Morimoto H, Tatsumisago M, Minami T. *Chem Lett*, 2001, 30: 872–873
45 Ujiie S, Hayashi A, Tatsumisago M. *Solid State Ion*, 2012, 211: 42–45
46 Ujiie S, Hayashi A, Tatsumisago M. *J Solid State Electrochem*, 2013, 17: 675–680
47 Ohtomo T, Hayashi A, Tatsumisago M, Kawamoto K. *J Non-Cryst Solids*, 2013, 364: 57–61
48 Hayashi A, Muramatsu H, Ohtomo T, Hama S, Tatsumisago M. *J Alloys Compd*, 2014, 591: 247–250
49 Tsujiwaki W, Higuchi E, Chiku M, Inoue H. *ECS Trans*, 2014, 58: 77–84
50 Zhang Z, Kennedy J. *Solid State Ion*, 1990, 38: 217–224
51 Yamauchi A, Sakuda A, Hayashi A, Tatsumisago M. *J Power Sources*, 2013, 244: 707–710
52 Hayashi A, Minami K, Ujiie S, Tatsumisago M. *J Non-Cryst Solids*, 2010, 356: 2670–2673
53 Seino Y, Ota T, Takada K, Hayashi A, Tatsumisago M. *Energ Environ Sci*, 2014, 7: 627–631
54 Mizuno F, Hayashi A, Tadanaga K, Tatsumisago M. *Solid State Ion*, 2006, 177: 2721–2725
55 Tachez M, Malugani J, Mercier R, Robert G. *Solid State Ion*, 1984, 14: 181–185
56 Liu Z, Fu W, Payzant EA, Yu X, Wu Z, Dudney NJ, Kiggans J, Hong K, Rondinone AJ, Liang C. *J Am Chem Soc*, 2013, 135: 975–978
57 Kanno R, Murayama M. *J Electrochem Soc*, 2001, 148: A742
58 Kamaya N, Homma K, Yamakawa Y, Hirayama M, Kanno R, Yonemura M, Kamiyama T, Kato Y, Hama S, Kawamoto K, Mitsui A. *Nat Mater*, 2011, 10: 682–686
59 Bron P, Johansson S, Zick K, Schmedt auf der Günne J, Dehnen S, Roling B. *J Am Chem Soc*, 2013, 135: 15694–15697
60 Kuhn A, Gerbig O, Zhu C, Falkenberg F, Maier J, Lotsch BV. *Phys Chem Chem Phys*, 2014, 16: 14669–14674
61 Rangasamy E, Liu Z, Gobet M, Pilar K, Sahu G, Zhou W, Wu H, Greenbaum S, Liang C. *J Am Chem Soc*, 2015, 137: 1384–1387
62 Tatsumisago M, Nagao M, Hayashi A. *J Asian Ceramic Soc*, 2013, 1: 17–25
63 Kanno R. *Solid State Ion*, 2000, 130: 97–104
64 Wang Y, Richards WD, Ong SP, Miara LJ, Kim JC, Mo Y, Ceder G. *Nat Mater*, 2015, 14: 1026–1031
65 Mo Y, Ong SP, Ceder G. *Chem Mater*, 2011, 24: 15–17
66 Ong SP, Mo Y, Richards WD, Miara L, Lee HS, Ceder G. *Energ Environ Sci*, 2013, 6: 148–156
67 Mercier R, Malugani JP, Fahys B, Robert G. *Solid State Ion*, 1981, 5: 663–666
68 Fan L, Zhuang HL, Zhang K, Cooper VR, Li Q, Lu Y. *Adv Sci*, 2016, 3: 1600175
69 Yuan S, Guo Z, Wang L, Hu S, Wang Y, Xia Y. *Adv Sci*, 2015, 2: 1500071
70 Hou TZ, Chen X, Peng HJ, Huang JQ, Li BQ, Zhang Q, Li B. *Small*, 2016, 12: 3283–3291
71 Nagata H, Chikusa Y. *J Power Sources*, 2014, 263: 141–144
72 Agostini M, Aihara Y, Yamada T, Scrosati B, Hassoun J. *Solid State Ion*, 2013, 244: 48–51
73 Nagao M, Hayashi A, Tatsumisago M. *J Mater Chem*, 2012, 22: 10015–10020
74 Nagao M, Hayashi A, Tatsumisago M. *Electrochim Acta*, 2011, 56: 6055–6059
75 Nagao M, Hayashi A, Tatsumisago M. *Energ Tech*, 2013, 1: 186–192
76 Yamada T, Ito S, Omoda R, Watanabe T, Aihara Y, Agostini M, Ulissi U, Hassoun J, Scrosati B. *J Electrochem Soc*, 2015, 162: A646–A651
77 Lin Z, Liu Z, Fu W, Dudney NJ, Liang C. *Angew Chem Int Ed*, 2013, 52: 7460–7463
78 Nagata H, Chikusa Y. *J Power Sources*, 2016, 329: 268–272
79 Chen M, Adams S. *J Solid State Electrochem*, 2015, 19: 697–702
80 Han F, Yue J, Fan X, Gao T, Luo C, Ma Z, Suo L, Wang C. *Nano Lett*, 2016, 16: 4521–4527
81 Kobayashi T, Imade Y, Shishihara D, Homma K, Nagao M, Watanabe R, Yokoi T, Yamada A, Kanno R, Tatsumi T. *J Power Sources*, 2008, 182: 621–625
82 Nagao M, Imade Y, Narisawa H, Kobayashi T, Watanabe R, Yokoi T, Tatsumi T, Kanno R. *J Power Sources*, 2013, 222: 237–242
83 Nagao M, Suzuki K, Imade Y, Tateishi M, Watanabe R, Yokoi T, Hirayama M, Tatsumi T, Kanno R. *J Power Sources*, 2016, 330: 120–126
84 Eom M, Son S, Park C, Noh S, Nichols WT, Shin D. *Electrochim Acta*, 2017, 230: 279–284
85 Xu R, Xia X, Wang X, Xia Y, Tu J. *J Mater Chem A*, 2017, 5: 2829–2834
86 Yao X, Huang N, Han F, Zhang Q, Wan H, Mwizerwa JP, Wang C, Xu X. *Adv Energ Mater*, 2017, 7: 1602923
87 Lin Z, Liu Z, Dudney NJ, Liang C. *ACS Nano*, 2013, 7: 2829–2833
88 Tanibata N, Tsukasaki H, Deguchi M, Mori S, Hayashi A, Tatsumisago M. *J Mater Chem A*, 2017, 5: 11224–11228
89 Xu R, Xia X, Li S, Zhang S, Wang X, Tu J. *J Mater Chem A*, 2017, 5: 6310–6317
90 Zhang C, Lin Y, Zhu Y, Zhang Z, Liu J. *RSC Adv*, 2017, 7: 19231–19236
91 Cheng XB, Zhang R, Zhao CZ, Wei F, Zhang JG, Zhang Q. *Adv Sci*, 2016, 3: 1500213
92 Cheng XB, Yan C, Chen X, Guan C, Huang JQ, Peng HJ, Zhang R,

Yang ST, Zhang Q. *Chem*, 2017, 2: 258–270
93 Sun Y, Zheng G, Seh ZW, Liu N, Wang S, Sun J, Lee HR, Cui Y. *Chem*, 2016, 1: 287–297
94 Whittingham MS. *Science*, 1976, 192: 1126–1127
95 Li L, Chen C, Yu A. *Sci China Chem*, 2017, doi: 10.1007/s11426-11017-19041-11421
96 Xin S, Chang Z, Zhang X, Guo YG. *Natl Sci Rev*, 2017, 4: 54−70
97 Guo Y, Li H, Zhai T. *Adv Mater*, 2017, 29: 1700007
98 Cheng XB, Hou TZ, Zhang R, Peng HJ, Zhao CZ, Huang JQ, Zhang Q. *Adv Mater*, 2016, 28: 2888–2895
99 Zhang R, Cheng XB, Zhao CZ, Peng HJ, Shi JL, Huang JQ, Wang J, Wei F, Zhang Q. *Adv Mater*, 2016, 28: 2155–2162
100 Cheng XB, Yan C, Huang JQ, Li P, Zhu L, Zhao L, Zhang Y, Zhu W, Yang ST, Zhang Q. *Energ Storage Mater*, 2017, 6: 18–25
101 Aurbach D, Zinigrad E, Teller H, Cohen Y, Salitra G, Yamin H, Dan P, Elster E. *J Electrochem Soc*, 2002, 149: A1267
102 Zhang R, Li NW, Cheng XB, Yin YX, Zhang Q, Guo YG. *Adv Sci*, 2017, 4: 1600445
103 Yang C, Fu K, Zhang Y, Hitz E, Hu L. *Adv Mater*, 2017, 29: 1701169
104 Cao R, Xu W, Lv D, Xiao J, Zhang JG. *Adv Energ Mater*, 2015, 5: 1402273
105 Liu QC, Xu JJ, Yuan S, Chang ZW, Xu D, Yin YB, Li L, Zhong HX, Jiang YS, Yan JM, Zhang XB. *Adv Mater*, 2015, 27: 5241–5247
106 Tao T, Lu S, Fan Y, Lei W, Huang S, Chen Y. *Adv Mater*, 2017, 5: 1700542
107 Luo W, Gong Y, Zhu Y, Li Y, Yao Y, Zhang Y, Fu KK, Pastel G, Lin CF, Mo Y, Wachsman ED, Hu L. *Adv Mater*, 2017, 29: 1606042
108 Zhang XQ, Cheng XB, Chen X, Yan C, Zhang Q. *Adv Funct Mater*, 2017, 27: 1605989
109 Zhang R, Chen XR, Chen X, Cheng XB, Zhang XQ, Yan C, Zhang Q. *Angew Chem Int Ed*, 2017, 56: 7764–7768
110 Zhang XQ, Chen X, Xu R, Cheng XB, Peng HJ, Zhang R, Huang JQ, Zhang Q. *Angew Chem Int Ed*, 2017, 56: 14207–14211
111 Hayashi A. *Solid State Ion*, 2004, 175: 683–686
112 Thangadurai V, Narayanan S, Pinzaru D. *Chem Soc Rev*, 2014, 43: 4714–4727
113 Chen X, Hou TZ, Li B, Yan C, Zhu L, Guan C, Cheng XB, Peng HJ, Huang JQ, Zhang Q. *Energ Storage Mater*, 2017, 8: 194–201
114 Nagao M, Hayashi A, Tatsumisago M. *Electrochem Commun*, 2012, 22: 177–180
115 Zhao CZ, Cheng XB, Zhang R, Peng HJ, Huang JQ, Ran R, Huang ZH, Wei F, Zhang Q. *Energ Storage Mater*, 2016, 3: 77–84
116 Yan C, Cheng XB, Zhao CZ, Huang JQ, Yang ST, Zhang Q. *J Power Sources*, 2016, 327: 212–220
117 Cheng XB, Peng HJ, Huang JQ, Zhang R, Zhao CZ, Zhang Q. *ACS Nano*, 2015, 9: 6373–6382
118 Cheng XB, Yan C, Peng HJ, Huang JQ, Yang ST, Zhang Q. *Energy Storage Mater*, 2018, doi: 10.1016/j.ensm.2017.1003.1008
119 Harada Y. *Solid State Ion*, 1998, 108: 407–413
120 Bohnke O. *Solid State Ion*, 1996, 91: 21–31
121 Itoh M, Inaguma Y, Jung W, Chen L, Nakamura T. *Solid State Ion*, 1994, 70-71: 203–207
122 Thangadurai V, Weppner W. *Ionics*, 2000, 6: 70–77
123 Ortiz GF, López MC, Lavela P, Vidal-Abarca C, Tirado JL. *Solid State Ion*, 2014, 262: 573–577
124 Aono H. *J Electrochem Soc*, 1993, 140: 1827–1833
125 Arbi K, Hoelzel M, Kuhn A, García-Alvarado F, Sanz J. *Inorg Chem*, 2013, 52: 9290–9296
126 Arbi K, Tabellout M, Lazarraga MG, Rojo JM, Sanz J. *Phys Rev B*, 2005, 72: 094302
127 Cretin M, Fabry P. *J Eur Ceramic Soc*, 1999, 19: 2931–2940
128 Martínez-Juárez A, Pecharromán C, Iglesias JE, Rojo JM. *J Phys Chem B*, 1998, 102: 372–375
129 Aono H. *J Electrochem Soc*, 1990, 137: 1023–1027
130 Cao C, Li ZB, Wang XL, Zhao XB, Han WQ. *Front Energy Res*, 2014, 2: 25
131 Cussen EJ. *Chem Commun*, 2006, 86: 412–413
132 Cussen EJ. *J Mater Chem*, 2010, 20: 5167–5173
133 Buschmann H, Dölle J, Berendts S, Kuhn A, Bottke P, Wilkening M, Heitjans P, Senyshyn A, Ehrenberg H, Lotnyk A, Duppel V, Kienle L, Janek J. *Phys Chem Chem Phys*, 2011, 13: 19378–19392
134 Kumazaki S, Iriyama Y, Kim KH, Murugan R, Tanabe K, Yamamoto K, Hirayama T, Ogumi Z. *Electrochem Commun*, 2011, 13: 509–512
135 El Shinawi H, Janek J. *J Power Sources*, 2013, 225: 13–19
136 Murugan R, Thangadurai V, Weppner W. *Angew Chem Int Ed*, 2007, 46: 7778–7781
137 Wang Q, Jin J, Wu X, Ma G, Yang J, Wen Z. *Phys Chem Chem Phys*, 2014, 16: 21225–21229
138 Yu X, Bi Z, Zhao F, Manthiram A. *Adv Energ Mater*, 2016, 6: 1601392
139 Judez X, Zhang H, Li C, Eshetu GG, Zhang Y, González-Marcos JA, Armand M, Rodriguez-Martinez LM. *J Phys Chem Lett*, 2017, 8: 3473–3477
140 Zhu Y, Li J, Liu J. *J Power Sources*, 2017, 351: 17–25
141 Wang Q, Wen Z, Jin J, Guo J, Huang X, Yang J, Chen C. *Chem Commun*, 2016, 52: 1637–1640
142 Tao X, Liu Y, Liu W, Zhou G, Zhao J, Lin D, Zu C, Sheng O, Zhang W, Lee HW, Cui Y. *Nano Lett*, 2017, 17: 2967–2972
143 Sheng O, Jin C, Luo J, Yuan H, Fang C, Huang H, Gan Y, Zhang J, Xia Y, Liang C, Zhang W, Tao X. *J Mater Chem A*, 2017, 5: 12934–12942
144 Fu KK, Gong Y, Hitz GT, McOwen DW, Li Y, Xu S, Wen Y, Zhang L, Wang C, Pastel G, Dai J, Liu B, Xie H, Yao Y, Wachsman ED, Hu L. *Energ Environ Sci*, 2017, 10: 1568–1575
145 Fu KK, Gong Y, Liu B, Zhu Y, Xu S, Yao Y, Luo W, Wang C, Lacey SD, Dai J, Chen Y, Mo Y, Wachsman E, Hu L. *Sci Adv*, 2017, 3: e1601659
146 Zhao CZ, Zhang XQ, Cheng XB, Zhang R, Xu R, Chen PY, Peng HJ, Huang JQ, Zhang Q. *Proc Natl Acad Sci USA*, 2017, 114: 11069–11074
147 Tikekar MD, Archer LA, Koch DL. *Sci Adv*, 2016, 2: e1600320
148 Lu Y, Tikekar M, Mohanty R, Hendrickson K, Ma L, Archer LA. *Adv Energ Mater*, 2015, 5: 1402073
149 Jin J, Wen Z, Wang Q, Gu S, Huang X, Chen C. *JOM*, 2016, 68: 2601–2606
150 Wang Q, Guo J, Wu T, Jin J, Yang J, Wen Z. *Solid State Ion*, 2017, 300: 67–72